



HAL
open science

Non-Invasive Raman and XRF Study of Mīnā'ī Decoration, the First Sophisticated Painted Enamels

Philippe Colomban, Gulsu Simsek Franci, Anh-Tu Ngo, Xavier Gallet

► **To cite this version:**

Philippe Colomban, Gulsu Simsek Franci, Anh-Tu Ngo, Xavier Gallet. Non-Invasive Raman and XRF Study of Mīnā'ī Decoration, the First Sophisticated Painted Enamels. *Materials*, 2025, 18 (3), pp.575. 10.3390/ma18030575 . hal-04918960

HAL Id: hal-04918960

<https://hal.science/hal-04918960v1>

Submitted on 18 Feb 2025

HAL is a multi-disciplinary open access archive for the deposit and dissemination of scientific research documents, whether they are published or not. The documents may come from teaching and research institutions in France or abroad, or from public or private research centers.

L'archive ouverte pluridisciplinaire **HAL**, est destinée au dépôt et à la diffusion de documents scientifiques de niveau recherche, publiés ou non, émanant des établissements d'enseignement et de recherche français ou étrangers, des laboratoires publics ou privés.

Non-invasive Raman and XRF study of mīnā'ī decoration, the first sophisticated painted enamels

Philippe Colomban^{1*}, Gulsu Simsek Franci², Anh-Tu Ngo¹, Xavier Gallet³

¹ MONARIS UMR8233, Sorbonne Université, CNRS, Campus Pierre-et-Marie Curie, 4 Place Jussieu, 75005 Paris, France;

² Department of Metallurgical and Materials Engineering, Faculty of Engineering, Istanbul Gedik University, Cumhuriyet Mah. İlkbahar Sok. No: 1 Kartal, 34876, Istanbul, Türkiye; gulsu.simsek@gedik.edu.tr

³ UMR 7194 – Histoire Naturelle de l'Homme Préhistorique (HNHP), Musée National d'Histoire Naturelle, CNRS, Université Perpignan Via Domitia, Musée de l'Homme, 17 Place du Trocadéro, 75116 Paris, France; xavier.gallet@mnhn.fr

* Correspondence: philippe.colomban@sorbonne-universite.fr

Abstract: Mīnā'ī wares, crafted during the (12th-13th centuries,) represent some of the earliest examples of sophisticated painted enamel decoration by potters. Due to the thinness of these enamel layers, their detailed characterization remains challenging, even with advanced techniques such as Proton Induced X-ray Emission (PIXE) and Rutherford Backscattering Spectrometry (RBS).

This study provides the first combined non-invasive analysis using X-ray Fluorescence (XRF) and Raman spectroscopy on five shards attributed to mīnā'ī wares. For comparison, two İznik shards from the 17th century, which feature similarly styled but thicker enamel decorations, were also analyzed. Interestingly, the mīnā'ī paste was found to contain lead and tin, suggesting the use of a lead-rich frit in its composition. This finding was confirmed through micro-destructive analysis using Scanning Electron Microscopy with Energy Dispersive Spectroscopy (SEM-EDS). Elements such as rubidium (Rb), strontium (Sr), yttrium (Y), and zirconium (Zr) produced significant XRF signals and effectively distinguished mīnā'ī ware from İznik ware.

A uniform tin-rich glaze, measuring (300-500 μm) in thickness, was used as a base layer for the much thinner painted mīnā'ī enamels. The colored areas (blue, turquoise, red, green, black, white, egg-plant) revealed the presence of various coloring agents and phases such as spinels, chromite, and ions like Cu²⁺ and Co²⁺, as well as opacifiers like cassiterite and lead-calcium/potassium arsenates). Two distinct cobalt sources were identified: one associated with arsenic, and the other with manganese and nickel. These cobalt sources are comparable to those used in İznik pottery. For the first time, boron was detected in the blue enamel of ~~Boron in blue~~ mīnā'ī ware.

Citation: To be added by editorial staff during production.

Academic Editor: Firstname Last-name

Received: date

Revised: date

Accepted: date

Published: date



Copyright: © 2024 by the authors. Submitted for possible open access publication under the terms and conditions of the Creative Commons Attribution (CC BY) license (<https://creativecommons.org/licenses/by/4.0/>).

Keywords: Iran; Seljuks; mīnā'ī; painted enamels; composition; pigments; Raman spectroscopy; pXRF; thickness; İznik; blue; white; fritware; boron; cassiterite.

1. Introduction

Mīnā'ī wares, produced during the 12th and 13th centuries, are regarded as the first sophisticated painted enamel decorations created by potters. These ceramics are considered among the most luxurious in the Islamic world [1-6]. According to McClary [7] and François [8], some argue that no evidence exists for mīnā'ī production before 1180 [5]. However, the Konya palace kiosk (the ancient capital of the Seljuk Sultanate, Türkiye), securely dated to the 1170s, was decorated with numerous mīnā'ī tiles. Production flourished in Iran until the early 13th century, ceasing with the Mongol invasion. Production cities are believed to include Kashan, Sava, Rayy, and Natanz [9,10].

The earliest Persian miniature manuscripts, dating back to the 12th century [11-13], display clear parallels with Seljuk mīnā'ī wares in terms of inspiration and technique.

Similarities with Chinese art are also evident in both pottery and manuscript decoration [10]. All *mīnā'ī* wares are thought to have been produced on stonepaste (fritware) bodies [2-10]. A well-documented recipe for stonepaste is found in a treatise written in 1301 (700 Hegira) by Kāshānī potter Abū'l-Qāsim, translated by Allan [14]. The recipe includes 10 parts quartz, called "sugary stone" (*shukar-i sang*), ground and sieved through coarse silk (corresponding to a grain size of 1-10 μm), combined with one part ground glass frit and [one-part](#) white clay. Holakooei [15] recently provided additional details on this process.

While most *mīnā'ī* wares are decorated over a white glaze, rare examples with turquoise-glazed bases exist. These, however, are limited and remain analytically understudied, particularly regarding their painted decorations. The most comprehensive study to date, employing Rutherford Backscattering Spectrometry (RBS) and Proton-Induced X-ray Emission (PIXE), was conducted by Nikbakht and Montazerzohouri in 2021 [16]. They highlighted the exceptional thinness of painted enamels, often just a few microns thick, applied over a glazed background. Their composition varied by color: PbO content ranged from 2-3 wt% for dark blue and black, up to 10 wt% for turquoise, and more than 30 wt% from cream, red, and some blues. SnO₂ content ranged from 4-10 wt% in cream and red but was absent in other colors. Notably, the authors acknowledged that these results include contributions from the deeper substrate, complicating the reliability of the analysis.

[The limitations of advanced techniques such as Rutherford Backscattering Spectrometry \(RBS\) and Proton Induced X-ray Emission \(PIXE\) for analyzing thin enamel layers motivated us to explore more accessible and increasingly portable methods \[17\], specifically portable X-ray fluorescence \(pXRF\) and Raman micro spectroscopy.](#)

[While XRF analysis shares some of the same uncertainties as PIXE—particularly regarding the depth of analysis in materials with layers of varying and often unknown thickness—Raman analysis offers greater control over the analyzed volume. By adjusting the illumination and light-collection optics, Raman spectroscopy can precisely target volumes ranging from cubic micrometers \(\$\mu\text{m}^3\$ \) to several cubic millimeters \(\$\text{mm}^3\$ \), with even broader areas accessible through mapping techniques.](#)

Recent preliminary non-invasive Raman spectroscopy studies on Persian pottery confirmed the variability in the glaze compositions of a *mīnā'ī* bowl depicting *Faridun astride the cow Birmaya*, dated to the mid-12th to early 13th centuries. Interestingly, cassiterite was present only in turquoise and green areas [17]. [The present study is](#) the first comprehensive [non-invasive](#) analysis of seven shards using both Raman microscopy and XRF.

[The accuracy of certain attributions requires further evaluation. Two of the examined samples, which share similar motifs as expected for *mīnā'ī* ware,](#) are believed to have been produced during a later period (i.e., post-16th century) at the Ottoman era İznik tile kiln workshops. A comparison will involve analyzing the glaze signatures using Raman spectroscopy alongside examining the chemical compositions of the glaze and pigments [with XRF](#). Previous studies have reported Raman spectra [18,19] of certain colored areas and provided body composition details for other samples [10,15,20,21].

2. Materials and Methods

2.1. Artefacts

Figure 1 illustrates the decorated surfaces of shards from the Soustiel's collection. Portion of this collection [has](#) been previously published [2,22]. The shards feature motifs resembling the horseman and sphinx decorations found in the British Museum (inv. 1930.0719.63) and the Metropolitan Museum of Art in New York [7]. In the 12th and 13th centuries, the sphinx was strongly associated with light and was regarded as a celestial creature of paradise [7,23]. Star motifs were also common, often appearing as star-shaped tiles [1-3,7]. Birds and peacock feathers frequently appeared in Persian poetry and miniatures [12,23,24]. However, peacock feather decorations (MP) are also associated with Damascus-style production in İznik [25]. The thickness of the black contours suggests a later production period, specifically the 17th century. The flower motif with a red-colored

center (MPP) is a distinctive feature of Íznik pottery, likely created by an Íznik potter [2,26]. Friezes were popular decorative patterns [12], with many motifs tracing back to the Sassanid era (3rd -7th centuries). Comparative analyses of these motifs are discussed in references [24,27-29].

2.2. Techniques

2.2.1. Optical microscopy

Sections and surfaces of each shard were observed without [any](#) preparation using a BX51 Olympus microscope equipped with 5x (NA: 0.15) and 10x (NA: 0.30) objectives and AnalySIS software (Olympus Soft Imaging Solution, Japan).

2.2.2. Scanning Electron Microscopy – Electron Dispersive Spectroscopy

After XRF and Raman analyses, small grains (less than $2 \times 2 \times 2 \text{ mm}^3$) were taken from shard corners for additional SEM-EDS analysis using a JEOL 5410LV SEM-EDX at 20 kV acceleration voltage. Samples were partially wrapped with carbon-rich conductive tape to minimize charging effects, leaving a [small, exposed](#) window for analysis. This method, while less effective than applying a conductive coating (C or Au-Pd) preserves the sample. The exposed window facilitates correlating Raman and SEM-EDS measurements, as recognizing specific-colored areas on SEM images can be challenging. EDS spectra were recorded at $\times 400$ magnification over a sub-millimeter area ($\sim 300 \times 250 \mu\text{m}^2$) much larger than the grain size, but these measurements cannot be considered average values. [The uncertainty of the measurement is less than 5 at.% for the major elements and 10 at.% for the minor ones.](#)

2.2.3. Portable X-ray Fluorescence Spectroscopy (pXRF)

The procedure followed is detailed in previous studies [30,31]. X-ray fluorescence (XRF) analysis was performed using a portable instrument (Elio, Milano, Italy) equipped with a miniature X-ray tube system featuring a Rh anode, a $\sim 1 \text{ mm}^2$ collimator, and a large-area Silicon Drift Detector with an energy resolution of $< 140 \text{ eV}$ for Mn $K\alpha$. The instrument detected an energy range from 1.3 keV (in air) to 43 keV. The instrument was positioned on a dedicated frame support, and measurements were conducted in point mode with a 180s acquisition time at 50kV and 80 μA , with no filter between the tube and sample. The analysis depth estimated using Beer–Lambert law, is defined here as the thickness of the top layer from which 90% of the fluorescence originates [32]. This depth is approximately 6 μm for Si $K\alpha$, 170 μm for Cu $K\alpha$, 300 μm for Au $L\alpha$, and 3 mm for Sn $K\alpha$. These values should be compared with the thicknesses of the painted enamels, which range from a few microns to several tens of microns [16,17,21].

Accuracy was checked by measuring reference glass and stone samples [30,31].

The intensities of the peaks of the electronic transitions ($K\alpha$, $K\beta$, $M\alpha$, $M\beta$, $L\alpha$, $L\beta$, $L\gamma$, etc.) giving the characteristic peaks depend firstly on the elements concerned and secondly on the contents of these elements. This is why, for example, the peak intensity of the major element Si (silicon) can be smaller than those of minor elements (e.g. Pb) and comparable to that of Rb traces. In addition, a complex-colored decoration requires a topological variation in the three dimensions of the coloring agent concentration. The calculus of a "composition", therefore, has no meaning, and this is why we developed the clustering analysis procedure in different diagrams comparing the areas of characteristic peaks. This procedure acquired in the analysis of hundreds of objects with Artax 7.4.0.0 (Bruker, AXS GmbH, Karlsruhe, Germany) software is described in previous papers [30,31,32,33]. The net area was calculated under the peak at the characteristic energy of each element selected in the periodic table, and the area of the major, minor and trace elements were determined in the colored areas. Before plotting the diagrams, the net areas of each element were normalized by the number of XRF photons derived from the peak of the X-ray tube of rhodium. In some cases, normalization with respect to the signal of another element (e.g. Co for blue area) was also made for comparison. Then, the data were

plotted in the ternary or biplot scattering diagrams. Additionally, Euclidian hierarchical similarity plots with average linkage (Ward's distance) were drawn for the interpretation and discussion of the results with Python software (version 3.12.4).

151
152
153
154
155



Figure 1. Studied samples decorated with a) two birds (MO, *mīnā'ī*, ~ 7x5.5x0.45 cm³), b) peacocks 156
feathers (MP, *Īznik*, ~ 7x4x0.3 cm³), c) a zig-zag black frieze (MFF, *mīnā'ī*, ~ 4x3x0.5 cm²) and d) a 157
flower (MPP, *Īznik*, ~ 2x1x0.55 cm³), e) a frieze of stars (MF, *mīnā'ī*, ~ 5x4x0.5 cm³), f) a blue sphinx 158
(MB, *mīnā'ī*, ~ 4x3x0.4 cm³) and g) horsemen figure (M, *mīnā'ī*, ~ 7.5x5x0.5 cm³); [bar: 1 cm](#). 159

2.2.4. Raman Microspectroscopy 160

Shards were analyzed in the laboratory using a Labram HR800 spectrometer 161
(HORIBA Scientific Jobin-Yvon, France) equipped with an Ar⁺ ion plasma laser Innova 162
I90C 6UV (Coherent Inc., Santa Clara, California, USA). 163

The 457.9 and 514.5 nm lines of Ar⁺ laser were employed at the laboratory with illu- 164
mination power at the sample surface ranging from approximately 0.3 mW (for colored 165
enamels) to 8 mW (for paste) for the blue line and from 0.2 mW to 2mW for the green line. 166
Comparison of the spectra facilitated the separation of vibrational and luminescence fea- 167
tures. A long working distance (LWD: 13 mm) 50× (NA: 0.45) microscope objective (Olym- 168
pus Corp., Tokyo, Japan) was used for analysis. Spot sizes were approximately 5 × 5 μm², 169
closely matching the expected pigment grain size. In-depth laser penetration was similar 170
for colorless glaze but significantly reduced for dark-colored areas. Spectral data were 171
recorded across a window of 50 to 4000 cm⁻¹. Counting times ranged from a few minutes 172
to several tenths of a minute, with at least three accumulations performed to suppress 173
cosmic ray signals. For each area considered, three spots were systematically analyzed. 174
Using a 600 lines/mm grating, the uncertainty in peak wavenumber was less than ±2 cm⁻¹. 175

3. Results 176

3.1. Microstructures

Figure 1 illustrates that most shards exhibit a crack network, indicative of poor compatibility between the thermal expansion coefficients of the glaze and the body. This suggests that the glaze was not optimised for quartz-rich body, possibly due to the use of glazes initially developed for other substrates. Visual examination led to assign MP and MPP shards to İznik kilns, the other shards being mīnā'ī wares.

Figure 2 presents photomicrographs of shard cross-sections. Some shards have a white paste (e.g., MF and MP), while others exhibit a pinkish tone. The fractures in most shards resemble that of a sugar cube (Figs. 2e, 2h and 2j), typical of fritware, where grains of sand are lightly cemented by intergranular glass. The mean grain size varies between $\sim 2 \mu\text{m}$ (MP, Fig. 2j) and $10 \mu\text{m}$ (MF, Fig. 2h). In contrast, the microstructure of MO appears denser and more glassy. The thickness of the base glaze layer, white or cream (M, MB, MF, MO and MP) and turquoise-blue (MPP) ranges from 200 to $500 \mu\text{m}$. The painted enamels are much thinner, approximately $100 \mu\text{m}$ for the red layer in photo 2f (MPP), with evidence of glaze diffusion into the paste. Black lines are even thinner, as seen in the surface views (Figure 3). A white background layer is clearly visible between the paste and the glaze in MPP (Figures 2a, 2d and 2f), consistent with production in İznik [2,17,25].

The painted enamel appears completely melted, as evidenced by the presence of bubbles (Fig. 3a) and segregation into islands resembling oil drops on a water surface (Fig. 3d). This suggests the use of a highly volatile flux, such as a boron-rich composition derived from borax, which forms very fluid phases when combined with lead oxide. The gilding is also thin, typically around one micron, as is standard practice [34]. In contrast, the surface of the MP sherd (İznik) displays a wrinkled and bubbled appearance due to its significantly greater thickness.

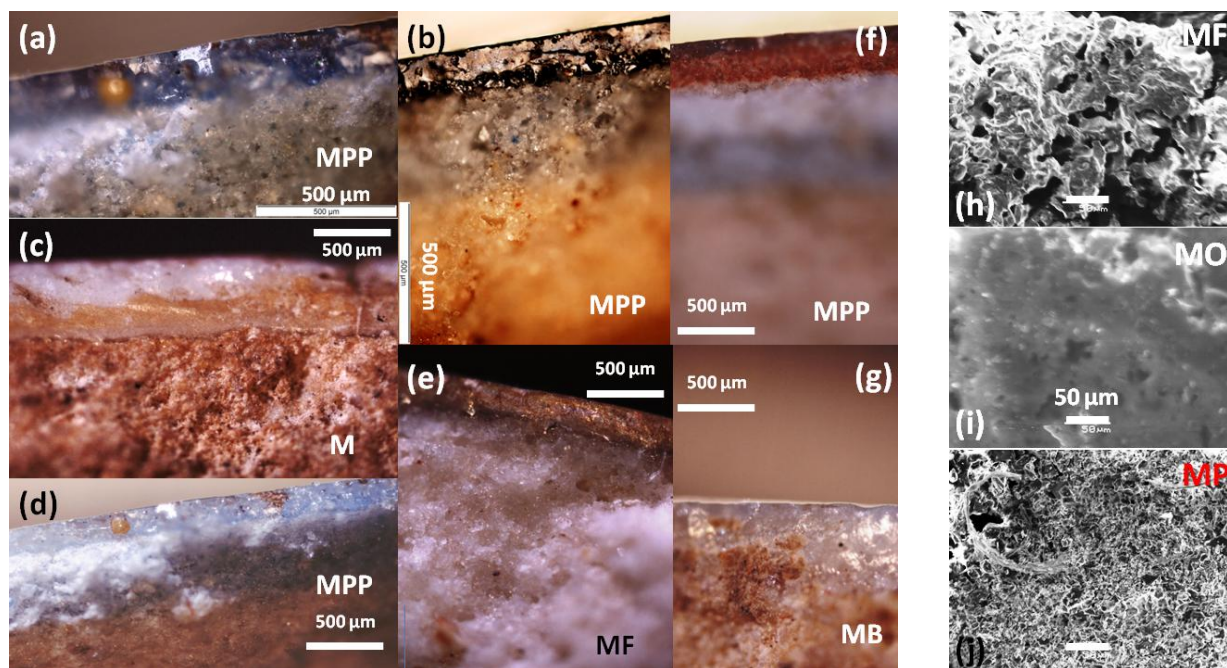


Figure 2. Selected optical views of shard sections (without polishing to preserve samples): a), b) and d) MPP blue background glaze (İznik), c) M horseman brown saddle glaze (mīnā'ī), e) MF frieze section with yellow background glaze (mīnā'ī), f) MPP red enamel on blue background (İznik), and g) MB sphinx blue background (mīnā'ī). SEM views of h) MF, i) MO and j) MP body fractures.

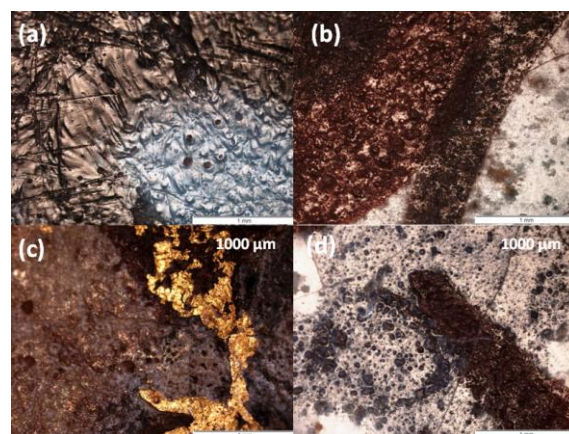


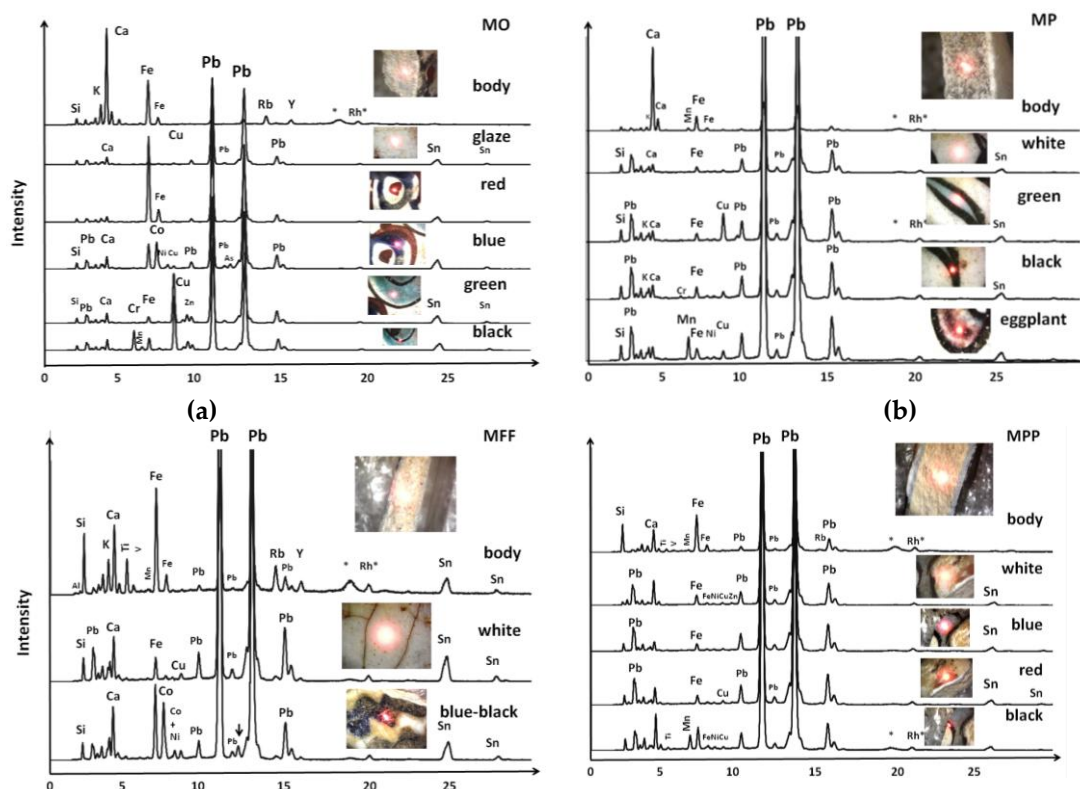
Figure 3. Selected optical surface views: a) green spot of the MP Peacock feathers (Īznik), b) red and black line of MO birds couple mīnā'ī shard, c) gold foils on MF frieze mīnā'ī shard and d) black line on blue enamel of MO birds couple mīnā'ī shard. 206
207
208

3.2. Information on elemental composition 209

Selected XRF spectra are shown in Figures 4 and 5. SEM-EDS spectra are shown in Figures 6 and 7. 210
211

3.2.1. Paste composition 212

Visual examination of the body spectra reveals differences in the relative intensities of the peaks for elements such as Ca, Fe, Si, Sn, and Pb. The variation in the intensity ratios of Fe K α /Si K α peaks is consistent with the two types of paste coloring: white (MF and MP) and pinkish (others). Calcium peak intensities are higher in MO, MP, and MB, while they are minimal in MPP and MF. Unexpectedly, some paste spectra show trace amounts of lead and tin, particularly in the M, MF, and MFF mīnā'ī shards. Traces of lead and tin are also detected in the MO and MB mīnā'ī shards. The pastes of the MP and MPP shards appear almost free of tin, consistent with some Īznik productions [35]. 213
214
215
216
217
218
219
220



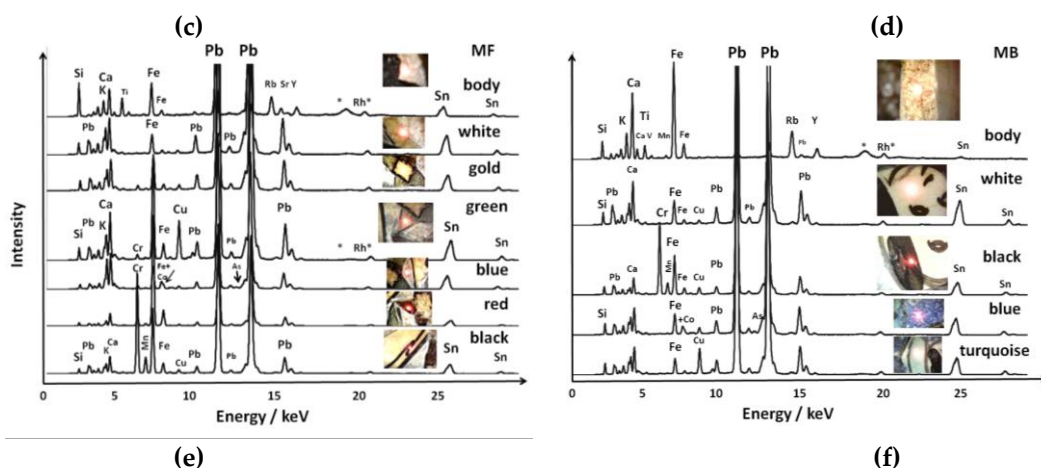


Figure 4. Selected XRF spectra of (a) two birds (MO, mīnāṭī), (b) peacocks feathers (MP, Īznīk), (c) a zig-zag black frieze (MFF, mīnāṭī), (d) a flower (MPP, Īznīk), (e) a frieze of stars (MF, mīnāṭī), and (f) a blue sphinx (MB, mīnāṭī). The spectra of lead-rich silicates have been amplified by a factor of 5 to 8 to enhance the visibility of peaks from other elements. Each analyzed area is visually represented, with the red spot marking the laser focus adjustment point. Peaks labeled with * and Rh* correspond to Compton scattering and the characteristic X-ray emission from the instrument anode, respectively.

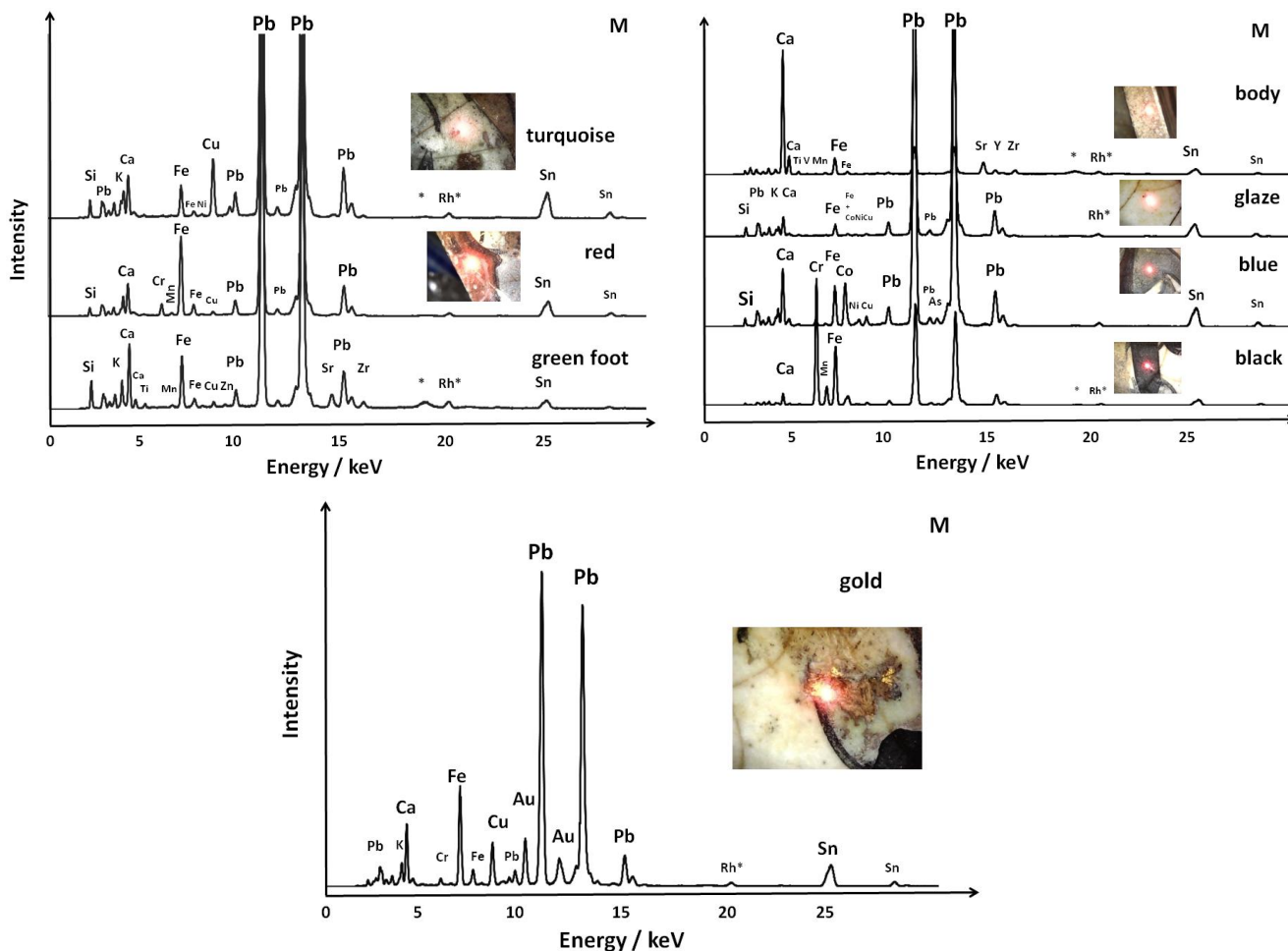


Figure 5. Selected XRF spectra recorded from different areas of the mīnāṭī shard depicting a horse-man (M). Some spectra of lead-rich silicates have been amplified by a factor of 5 to 8 to highlight the peaks of other elements.

221
222
223
224
225
226
227

228
229
230

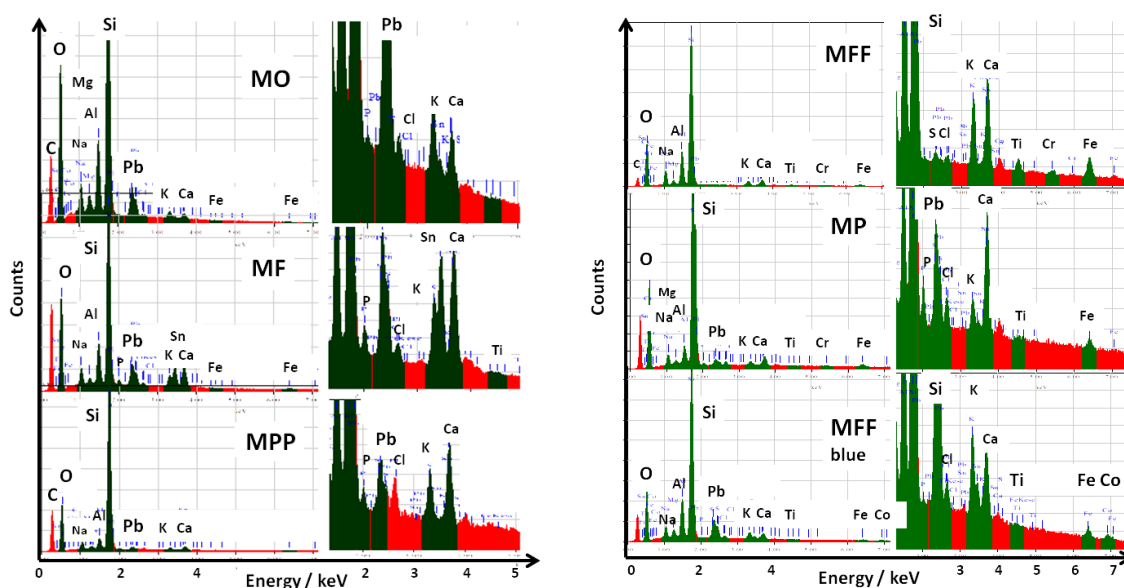


Figure 6. Selected SEM-EDS spectra from the paste (fractures of MO and MF mīnā'ī shards and MPP and MP Īznik shards) and the blue area of MFF. Zoomed-in views of the 1 to 5 keV spectral range are shown on the right side.

The EDS spectra (Figure 6) and the calculated compositions (Table 1) confirm the XRF analyses: the pastes are highly siliceous, particularly for Īznik shards, with sodium being the main flux. Small quantities of lead and tin are detected. SEM-EDS measurements made at a much smaller scale ($\sim 7.5 \cdot 10^{-2} \text{ mm}^2$) than XRF analysis show the heterogeneous distribution of tin and lead. The mean composition of mīnā'ī paste, calculated from the data in Table 1, is approximately at % Si: 25.3 Al: 3.5 Mg: 0.77 Na: 3.39 K: 0.77 Ca: 0.92 Pb: 1.17 Sn: 0.36. This corresponds to the following wt% oxide composition: wt% 62 SiO₂ - 14.5 Al₂O₃ - 1 MgO - 5.5 Na₂O - 3 K₂O - 2 CaO - 10.5 PbO - 2 SnO₂. These values are in good agreement with previous data [16,35-37], except for the significantly higher aluminum content. [Īznik productions from the 16th and 17th centuries are characterized by a high quartz content \(65–85% SiO₂\) and low alumina levels \(3–6 wt% Al₂O₃\), reflecting the typical fritware/stonepaste recipe commonly used in the production of "Īznik" tiles \[35\]. The findings shown in Table 1 confirm that MP and MPP belongs to the group of Īznik productions.](#) –The decision to avoid quartz grains in the EDS measurement likely contributed to the elevated aluminum levels observed. Indeed, a considerable compositional heterogeneity (a factor >2 for some element) is observed within the same sample. Iron content is low, and the high amount of silica in the Īznik shard is highlighted by the large number of quartz grains.

Table 1. Local compositions (at %) measured by SEM-EDS for different spots on the body fracture at 400x magnification ($\sim 300 \times 250 \mu\text{m}^2$ area). Full data are provided in Appendix A ($\Sigma = \text{Na} + \text{K} + \text{Ca}$).

Shard	Type	Si	Al	Si/Al	Mg	Σ	Pb	Sn	Pb/Sn	P	Fe	Ti	Co	Cr
MPP1	Īznik	19.29	2.85	6.77	0.31	6.29	3.22	0.31	10.4	0.43	0.02	-	-	-
MPP2+	Īznik	9.26	4.38	2.11	0.62	4	2.13	0.04	53.2	4.26	0.03	0.03	-	-
MPP3	Īznik	31.98	1.65	19.38	0.24	3.64	0.23	-	-	0.43	0.15	-	-	-
MP1 ^a	Īznik	37.8	1.21	31.24	0.38	2.89	0.23	-	-	0.4	0.55	0.05	-	0.15
MP2	Īznik	35.77	1.21	29.56	0.31	3.03	0.54	0.05	10.8	0.72	0.21	0.03	-	-
MO1 ^b	mīnā'ī	25.04	3.49	7.17	1.33	6.09	1.85	0.38	4.86	0.17	0.53	0.01	0.19	0.13
MO2	mīnā'ī	20.57	4.6	4.47	1.04	4.22	1.15	0.13	8.84	0.10	0.02	0.02	-	-
MFF1	mīnā'ī	25.58	3.61	7.09	1.68	8.45	2.6	1.23	2.1	0.15	0.15	0.02	-	-
MFF2	mīnā'ī	28.09	5.69	4.94	0.81	6.48	-	-	-	0.15	0.58	0.22	-	0.08
MFF3 ^c	mīnā'ī	27.06	5.54	4.88	1.24	5.24	1.89	0.39	4.85	0.14	0.23	0.03	0.14	-
MF1	mīnā'ī	25.52	4.34	5.88	0.55	5.1	-	-	-	0.14	0.21	0.23	-	-

MF2	mīnā'ī	18.37	3.61	5.09	0.64	5.29	1.17	1.89	0.61	0.65	0.29	0.04
-----	--------	-------	------	------	------	------	------	------	------	------	------	------

+ magnification: 2000x; ^a : close to the black glaze; ^b close to the blue glaze; ^c close to the blue glaze.

The presence of tin does not result from contamination during the firing of lead-based enamels, as the measurements were made on the breakage of the shards, most of them far away from surface. Moreover, tin is detected in most of the spots. It is plausible that the tin originates from the lead source used, likely waste from bronze manufacturing, as Persian bronzes were made from copper-tin alloys containing approximately 20 % lead [36]. To our knowledge, the presence of tin in the mīnā'ī paste, undoubtedly sourced from the lead-rich frit glass, has not been highlighted previously. The Pb/Sn ratio ranges from 0.5 to 50, with the central distribution between 4 and 10, which is consistent with the ratio of 5 observed in Persian bronze [36]. The inability to polish the small fragments (~1 to 5 mm³) from certain shards means that the proportion of the vitreous phase and its distribution between quartz grains cannot be fully observed. The area analyzed is relatively large compared to the grain sizes (~300x250 μm² versus ~1 to 20 μm in grain diameter), but significant compositional heterogeneities are observed (as seen in the different measurements on the same shard). For example, calcium content varies by a factor 3 (MF mīnā'ī) or 4 (MPP Īznik), while sodium content varies by a factor 2 (MPP Īznik). The MP1 shard stands out for its lower flux content, which is compensated by a much finer grain size, facilitating sintering. Aside from the higher silica content, similarities between Ottoman and mīnā'ī pastes are also noted.

Measurements taken near the glaze reveal small amounts of cobalt and chromium, likely due to the intrusion of the enamel as it melts into the cracks and porosity of the paste. This behavior is consistent with the low viscosity of the enamel at firing temperature and the thinness of the painted decoration.

The significant presence of phosphorus in some of the shards appears too high (up to 2.5 at %, with mean values of ~0.5 and 0.15 for Īznik and mīnā'ī paste, respectively) to be attributed solely to contamination from prolonged exposure in the ground (since the objects come from excavations). This phosphorus suggests the use of raw materials containing phosphate. The incorporation of bone into glass production was practiced by Sasanian glassmakers [38], and these glasses also contain small amounts of sulfur and chlorine. Such glass may have been used to prepare the frit used for cementing sand.

3.2.2. Glaze composition

Due to the interdiction of sampling from other areas than the corner of one Īznik shard (MPP, see Appendix A, Table 1B), pXRF measurements were taken from the upper surface of the shards.

3.3. Classification from composition ratios measured by pXRF

Figures 7 and 8 compare ternary diagrams built from the areas of the peaks related to the elements with visible pXRF peaks.

3.3.1. Body

The Pb-K-Ca ternary diagram visualizes the variability in lead content as detected by pXRF (Fig. 7a). The measurements reveal at least two types of paste: MF and MFF are lead-rich, while MP, MB, M and MO contain more calcium. This relationship between mīnā'ī and Īznik pastes is confirmed. MPP and MP shards, however, show the lowest potassium content, clearly differentiating the two types of ceramic bodies.

The examination of signals related to impurities, such as Rb and Sr (Fig. 7b), and Zr, Sr, and Y (Fig. 7c) (whose XRF signals are significant even at low concentrations and thus serve as reliable markers), further confirms the distinctions between groups. The levels of earth-alkaline impurities (e.g., Sr) corroborate the division of mīnā'ī shards into three groups: MO and MB (first group), M and MF (second group), and MFF (third group), with MPP and MP being associated with Īznik production. Zr-Sr-Y ternary diagram (Fig. 7c)

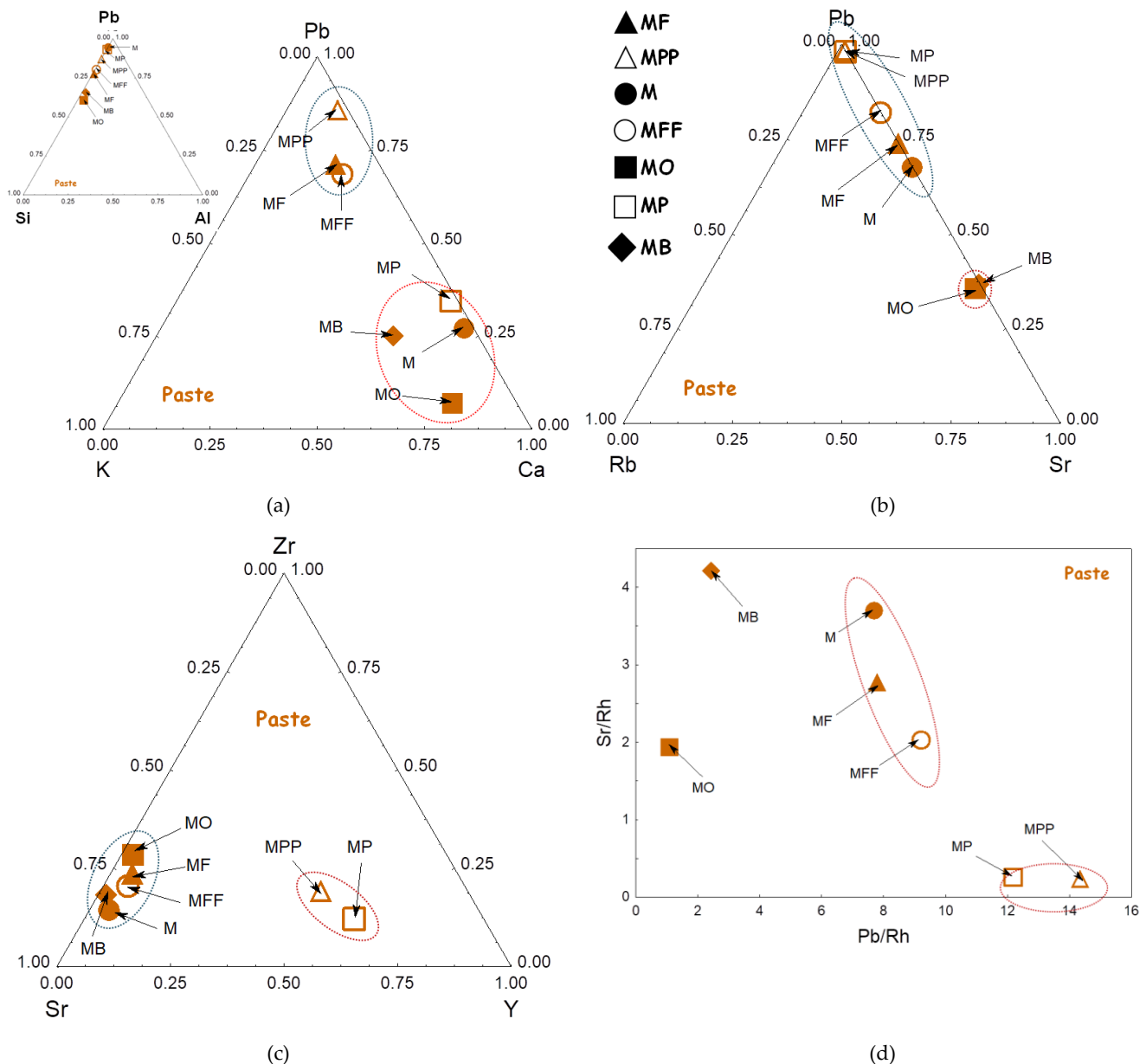
and the Sr vs Pb scattering biplot support this classification demonstrating the efficiency of pXRF in distinguishing pastes based on impurities from raw materials.

The ternary diagram based on Pb, Sn, and Si signals (Fig. 7e) further supports classification, with the mīnā'ī group (MO, M, MB, MF, and MFF) exhibiting higher tin content.

3.3.2. Background glaze

The Pb-Sn-Si diagram (Figure 7e) does not differentiate between the glazes covering the paste. However, the Sn/Rh vs. Pb/Rh scattering biplot (Fig. 7f) successfully identifies the two groups already distinguished from paste analyses: MP and MPP Īznik shards on one side, and the other shards on the other side.

However, the Sr/Rh vs. Pb/Rh scattering biplot (Fig. 7d) also reveals three groups within the mīnā'ī paste: one group consists of M, MF, and MFF shards, while the MB and MO shards are sufficiently distinct to belong to separate groups. This suggests the use of different raw materials, likely indicating different production locations or time periods. More samples are needed to obtain a further conclusion.



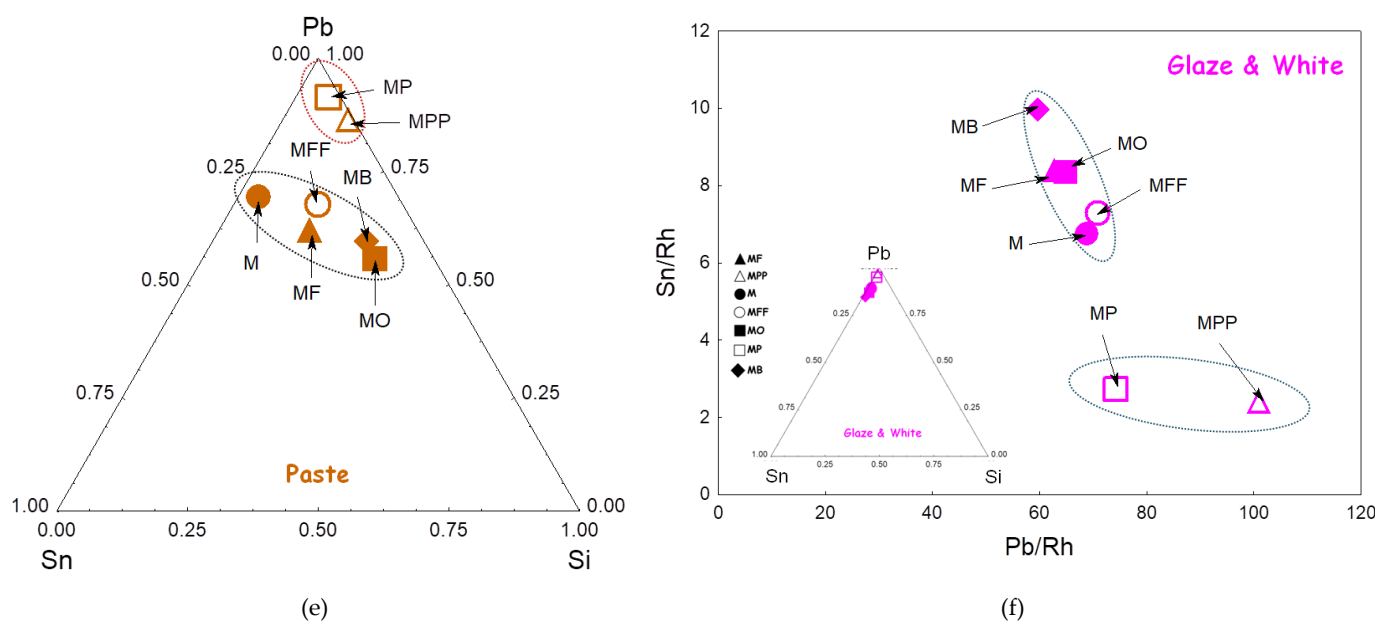


Figure 7. Comparison of the peak area for Pb, K and Ca flux elements (a), Pb and Rb and Sr impurities (b) Zr, Sr and Y (c) impurities as well as Sn vs Pb in the body (e) and in the glaze (f). 319 320

3.3.3. Cobalt and associated elements 321

Figure 8 compares the peak areas characteristic of cobalt, the blue chromophore, and associated elements characteristic of primary type mine deposits (Mn) or hydrothermal veins (As, Bi, Figs 8a-b). Nickel is common to both types of geological context and less efficient (Fig. 8c) to classify cobalt sources [39,40]. Two groups are clearly identifiable, on the one hand MF, M, MO and MB *mīnā'ī* shards which use cobalt associated with arsenic and MPP *Īznik* one whose cobalt is associated with manganese and nickel, like the bluish flow on the foot of the M sherd (probably a contamination during the firing in the kiln). It also contains bismuth (Fig. 8b). Bi-Mn-As ternary scattering diagram classifies very well two groups: M, MB and MF in one hand and MO, M and MFF in the other. 322 323 324 325 326 327 328 329 330

The black color ones are based on manganese but contain also some cobalt, bismuth and nickel. 331 332

Ores collected from the site of some of the ancient Iranian mines [41] were studied by Matin and Pollard [42,43]. The ores contain arsenic which is compatible with the measurements, but nickel and bismuth have not been measured by Matin and Pollard. 333 334 335

3.3.4. Other colors and luster 336

The impurity diagrams (Fig. 8e-f) do not provide any clear discrimination criteria. Traces of silver are detected in the red areas of MO, M, and MF shards, which may indicate that some parts underwent a luster-type preparation [44,45] that has since degraded over time. Luster has been reported in *mīnā'ī* wares [2,16]. 337 338 339 340

Gilding was applied using pure gold for the M shard, but with an alloy of gold and silver for the MF shard (Fig. 8e). 341 342

The red color is derived from iron, while the purple/eggplant color is attributed to manganese (Fig. 8f). 343 344 345

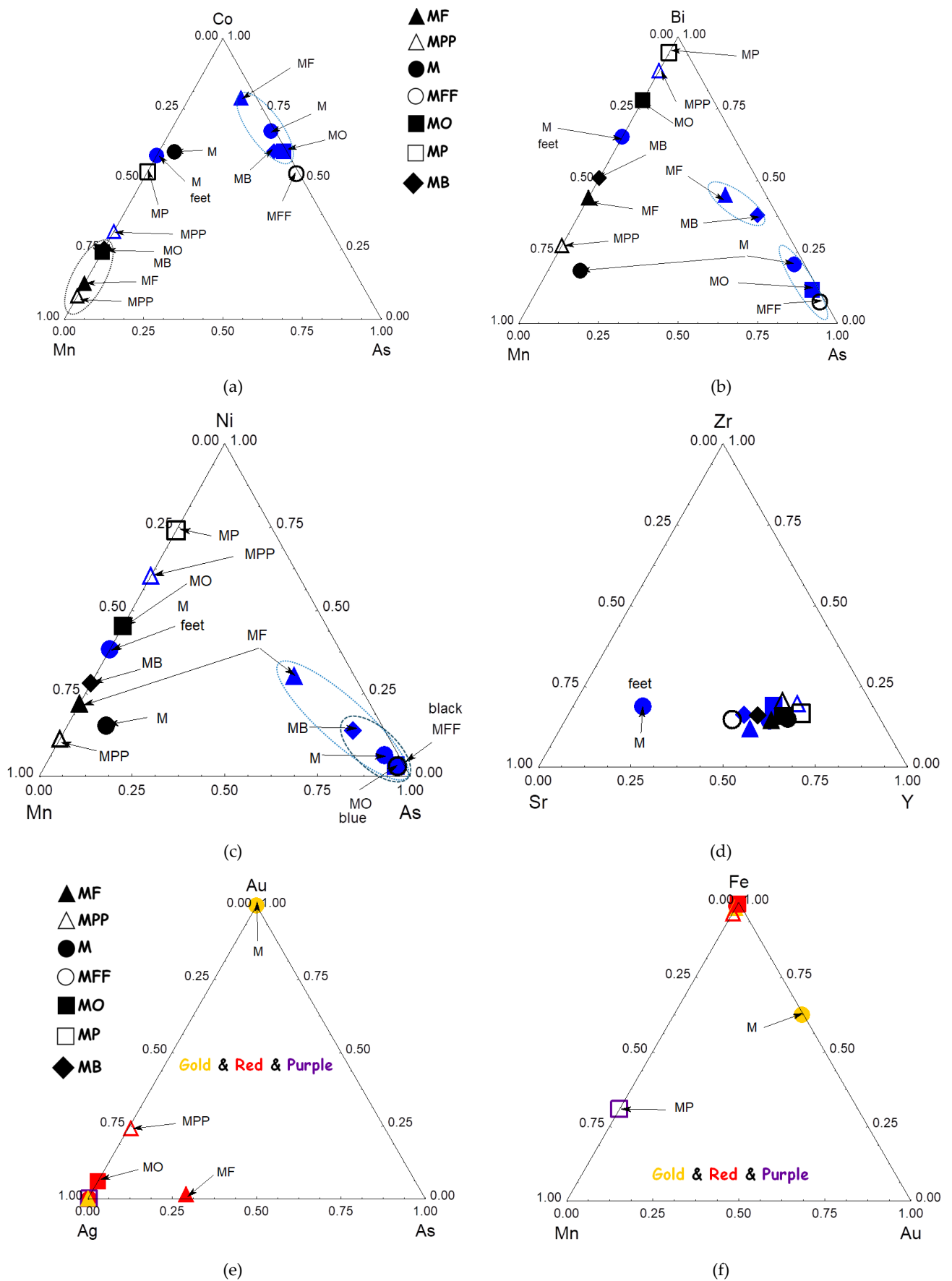


Figure 8. Comparison of the peak area for Co and associated elements (a, b and c), of glassy matrix impurities (d) and of chromophore and associated elements for red, purple and gilding.

3.4. Phase characterization

Simple elemental analysis does not make it possible to identify in what form the coloring element is found. Selected Raman spectra recorded on different spots of the shards are shown in Figures 9 to 11.

3.4.1. Body Raman signatures

Raman spectra firstly show the very characteristic spectrum of quartz with stronger $\sim 465 \text{ cm}^{-1}$ peak (bending SiO_4 mode), broad librational mode at $\sim 200 \text{ cm}^{-1}$, lattice mode at 100 cm^{-1} and series of narrow small peaks between 200 and 1155 cm^{-1} as previously observed [46] (see examples of nearly 'pure' quartz spectrum on Figs 9c and 9d). Additionally, spectra characteristic of titanium oxide, rutile (broad bands at 255, 420 and 605 cm^{-1} , Fig. 9a) and anatase (strong narrow peak at 144 cm^{-1} and broader at 400 and 505 cm^{-1} [47]) are observed according to the detection of titanium by SEM-EDS (Table 1). Due to the huge Raman intensity of these phases, these Raman signatures are observed in many potteries [48]. Calcite with its characteristic narrow 1085 cm^{-1} peak [49] is detected in M (Fig. 9a) and MP (Fig. 9b) samples according XRF measurements (Figures 5 and 4). In the latter shard, body gypsum is observed (narrow peak at $\sim 1005 \text{ cm}^{-1}$ and smaller at 180, 412, 490, 610 and 1130 cm^{-1} [50], Fig. 9b) according to detection of sulfur by EDS (Table 1a, Appendix A). The strong peak at 945 cm^{-1} (Fig. 9a, Fig. 9b) might correspond to a phosphate [51,52], phosphorus being detected by SEM-EDS (Table A1a, Appendix A).

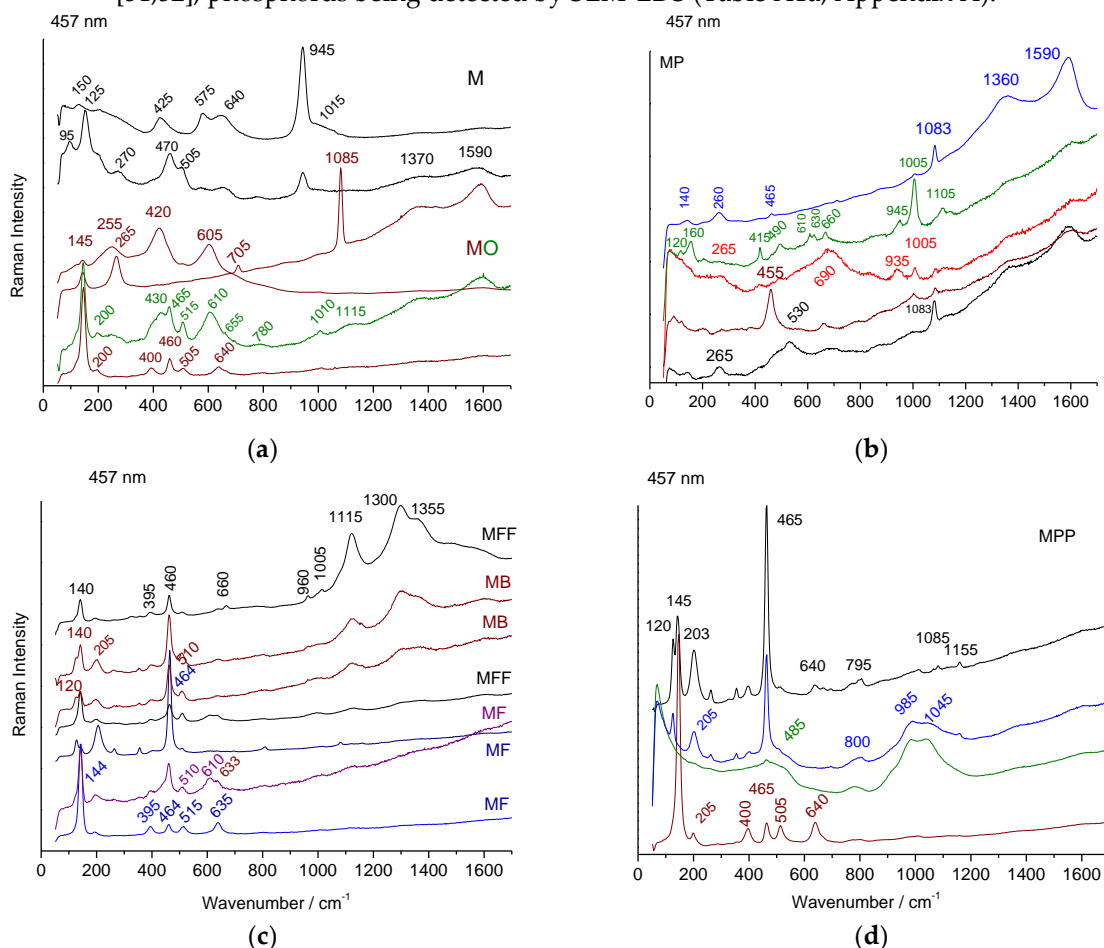


Figure 9. Selected Raman spectra recorded under blue laser excitation in different points of the body fracture section of M (a), MO (a), MP (b), MB (c), MF (c), MFF (c) and MPP (d) shards.

Spectra characteristics of a glassy phase are recorded in some spots (Fig. 9b). The center of gravity of the stretching band of SiO_4 tetrahedron, the main vibrational unit of silicate [53,54] ranges between 985 and 1045 cm^{-1} that corresponds to mixed lead-alkali

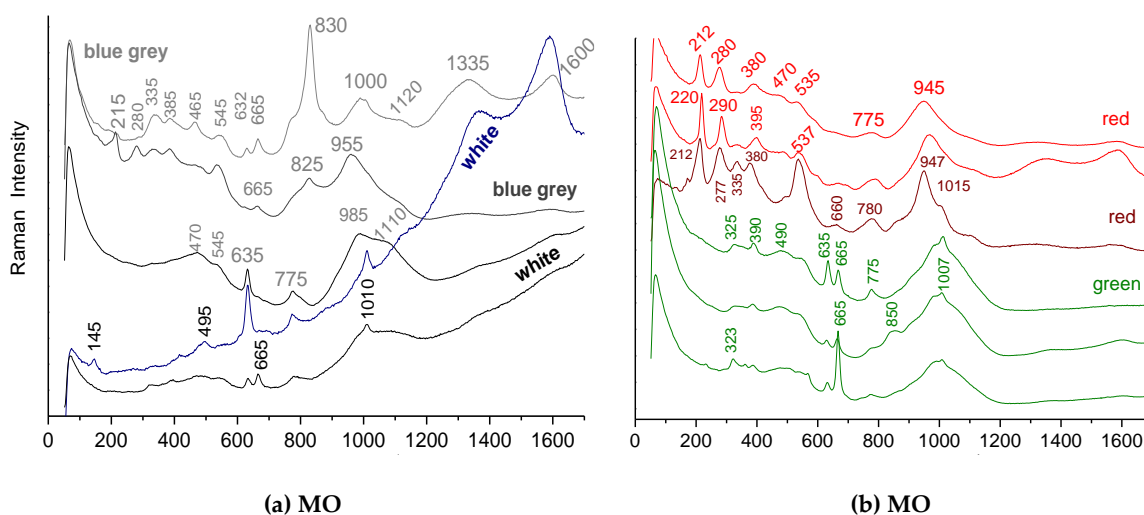
glass composition [17,35] according to composition measurement (Table 1). Cassiterite that is characterized by a narrow peak at 633 cm^{-1} and a smaller one at 775 cm^{-1} [17,55], is only clearly detected in MP (Fig. 9a) and MF (Fig. 9c) shards, at very low intensity. Spectra characteristics of black spinel (MO, Fig. 9a) are also detected according the detection of iron, manganese and chromium by XRF or SEM-EDS in the paste. A strong doublet is observed at 1115 and 1300 cm^{-1} in MB and MFF samples (Fig. 9c). This feature is similar to the luminescence observed in calcium-rich glass/glaze, especially those with nucleation of wollastonite (CaSiO_3) [56,57].

3.4.2. Raman signatures of glaze and painted enamels matrices

Figures 10 and 11 compare selected Raman spectra recorded from the surface of the glazed background and the painted decorations.

The $635\text{--}775\text{ cm}^{-1}$ doublet of cassiterite is observed in all shards except MP and MPP Āznik shards (Figure 10), despite EDS detecting tin concentrations between 0.14 and 0.29 at % in the MPP blue glaze (Table A1b, Appendix A). This suggests that tin can remain dissolved in the glassy silicate phase, consistent with its incorporation as a lead impurity. Previous studies on early Āznik production have shown that tin can be dissolved in the glaze at levels up to approximately 5–7 wt % SnO_2 [44,58].

The Raman spectrum of a glassy silicate provides insight into the degree of polymerization of the SiO_4 tetrahedron, the structural and vibrational unit of silicates, whether crystalline or amorphous [53,54]. The center of gravity of the SiO_4 stretching band ranges from ~ 950 (e.g., red areas in MO shard, Figure 10b) to 1020 cm^{-1} (e.g., green areas in MO shard, Figure 10b), corresponding to a lead-rich glass at the lower energy end and mixed lead-alkali glass at the higher energy end [17,53,54]. The polymerization index (I_p) derived from the ratio of the bending to stretching modes of SiO_4 [53,54] ranges from 0.3 (red) to 0.5 (green). These values correspond to glazes with varying melting behaviors and, consequently, different firing temperatures [53,54], typically between approximately ~ 600 and $\sim 800^\circ\text{C}$. For most colors, these values align with those observed in a prior study of a bowl [17] depicting *Faridun astride the cow Birmaya*. However, in that bowl, the background glaze was nearly free of lead, with a primary stretching mode at 1100 cm^{-1} . The Āznik glaze Raman signature of the stretching band (Figs. 10e and 10f) shows the characteristic $985\text{--}1040\text{ cm}^{-1}$ doublet [17,46].



(a) MO

(b) MO

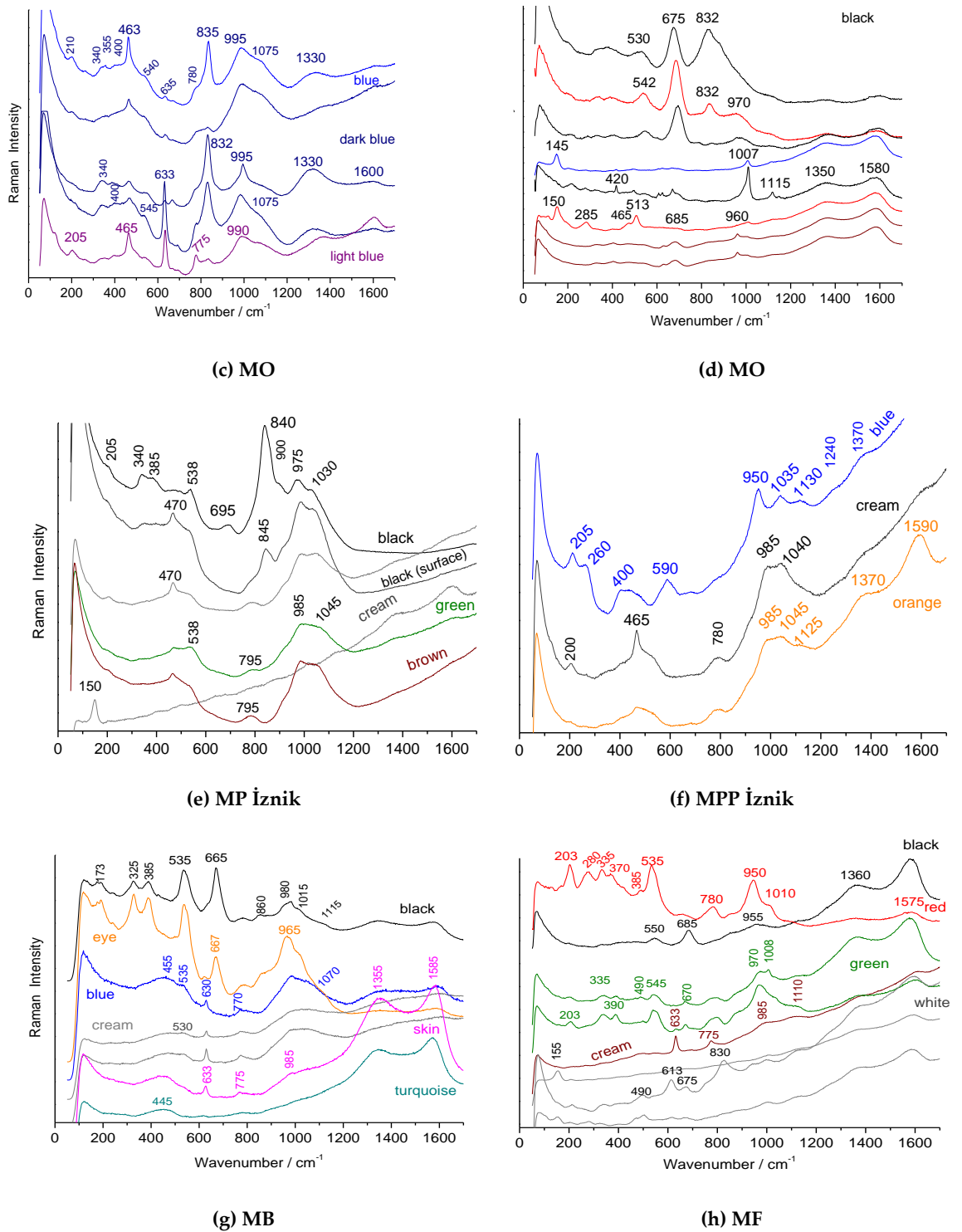


Figure 10. Selected Raman spectra recorded using a blue laser at various points on the shard surfaces of MO (a, b, c and d), MP (e), MPP (f), MB (g) and MF (h).

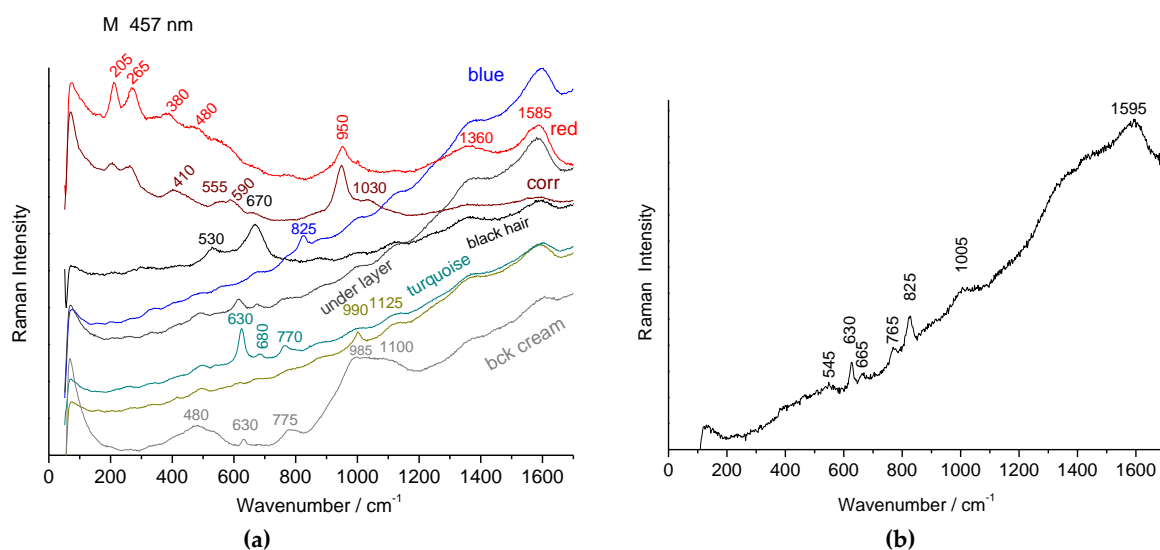


Figure 11. Selected Raman spectra recorded with blue laser in different points of the shard surface of M (a, b,) shard (b, face).

3.4.3. Pigment Raman signatures

The peak observed between 815 and 830 cm⁻¹ (Figs. 10a and 10c, Table 3), characteristic of lead-potassium-calcium-sodium arsenates (various phases are possible, with their signatures being rather similar [59]), appears in the blue regions and is consistent with the use of Kashan cobalt ores. In many areas (Figure 10c), the AsO₄ ion signal is absent. Since this signature is not detected throughout all points of the blue zones, it is likely that the blue color arises from the 'simple' dissolution of Co²⁺ ions in the silicate glass network, accompanied by some precipitation of arsenic-rich phase(s). Destructive Transmission Electron Microscopy or Synchrotron-μ X-ray diffraction will be required to gain a comprehensive understanding of the different phases and their distribution in the glazed layer.

Spectra obtained from the dark blue-colored regions using a blue laser excitation reveal an additional intense peak around 1250–1350 cm⁻¹ (Fig. 10c), typical of enamels where borax is expected to have been added [60]. This peak corresponds to B-O stretching modes, which appear in this spectral range [61–64]. Matin and Pollard identified the mineral ulexite (NaCaB₅O₉•8(H₂O)) associated with Kashan cobalt ores [42,43]. Borax acts as a highly effective flux, enabling low-temperature fusions and reducing viscosity. Its use is well documented in the preparation of blue-painted enamels in the 18th century on both soft and hard porcelain, in Europe and China [60,65,66]. Furthermore, borax was widely used in the decoration of İznik wares (16th century) [67] and in the preparation of certain Chinese glass objects (Liao Dynasty, 10th–12th centuries) [68]. The use of borax in the production of blue-painted enamels, though undoubtedly unintentional as it originates from the cobalt source, represents an important discovery. The dual association of arsenic and borax in Kashan cobalt ore is particularly advantageous for enameling.

Raman spectra of black regions reveal the signature of chromate ions at 840 cm⁻¹ (Figs 10d and 10e) [17,40,46]. In other cases, chromate is not detected, but a typical spinel signature (main peak at ~670 cm⁻¹, Figs 10d and 10g) is observed, corresponding to a phase based on Mn and Fe [40,69].

Red areas exhibit the signature of hematite, with a series of peaks at ~200, 280, 390 cm⁻¹ (Figs 10b and 11a), among others [70].

For turquoise and green colors, only glass spectra are observed, with the enamel colored by Cu²⁺ ions without the formation of a crystalline phase (Fig. 10g).

Table 4 lists the crystal phases identified.

Some of the enamels exhibit a peak around 950 cm⁻¹ (M, MPP, MF, Figs 10b, 10h and 11a), which is too sharp to correspond to the SiO₄ stretching mode of the glassy phase and

is more likely indicative of a phosphate [51,52], as SEM-EDS measurements reveal a strong phosphorus signal for these shards. 442
443

Table 2. Characteristic Raman peak wavenumbers used to identify pigments and opacifiers and main components of the SiO₄ stretching modes. 444
445







Samples		cream	white	dark blue	blue	light blue	red	brown	green	turquoise	black	
dimension (cm)	M											
 MO		150				633-775					542	
7x5.5x0.45		513		832	835	832					675	
		685		995	995	990					832	
		960		1330	1330	1330					970	
		1007										
		1115										
 MP (Iznik)								985	985		840	
7x4x0.3								1045	1045		975	
											1030	
 MPP (Iznik)					985				985			
2x1x0.55					1045				1045			
 MF		633-775	613				200		545		550	
		985	830				280		970		685	
	5x4x0.5			675				535		1008		955
								950				
								1010				
 MB					633-775					475	500	
					820					985	655	
					9555					1120	950	
	4x3x0.4					1120						
 M												
7.5x5x0.5												

Table 3. Pigments and opacifiers. 446
447

shard	MO	MP (Iznik)	MF	MPP (Iznik)	MB	M	Bowl [17]
White	cassiterite		anatase? arsenate		cassiterite arsenate	-	
Cream			cassiterite	anatase	cassiterite	cassiterite	
Blue	arsenate			phosphate	cassiterite	arsenate	
Turquoise					no	cassiterite	cassiterite
Red/brown	hematite	-	hematite		-	hematite	
Orange		-					
Green		anatase	cassiterite			-	cassiterite

Black	chromite	spinel	chromite	spinel	spinel
-------	----------	--------	----------	--------	--------

448

As observed when comparing the ternary diagrams for the major elements, the similarities between the pastes of mīnā'ī and Īznik make hierarchical classification ineffective (Figure 12a) when using these variables. However, the use of impurities that give a significant signal in XRF is effective (Figure 12b). This indicates the use of certain specific raw materials for each group. Classification based on cobalt and its associated elements (Figure 12c) imperfectly categorizes mīnā'ī shards if all blue-colored areas are considered but perfectly does so when only the decorative areas are considered. Figure 13, which compares the cobalt signals and associated elements obtained for mīnā'ī decorations with all the data collected on various Īznik productions, mainly tiles [35,67,68], shows that the light blue and dark blue areas belong to the same groups as those for Īznik decorations. These groups are characterized either by an association with manganese, in addition to nickel and zinc with arsenic, while iron is always present. Thus, there are two types of cobalt sources (associated with Mn and As respectively). The exclusive use of cobalt associated with arsenic for light blue areas indicates that Iranian potters understood the benefit of arsenic as an opacifier, enhancing the blue color.

449
450
451
452
453
454
455
456
457
458
459
460
461
462

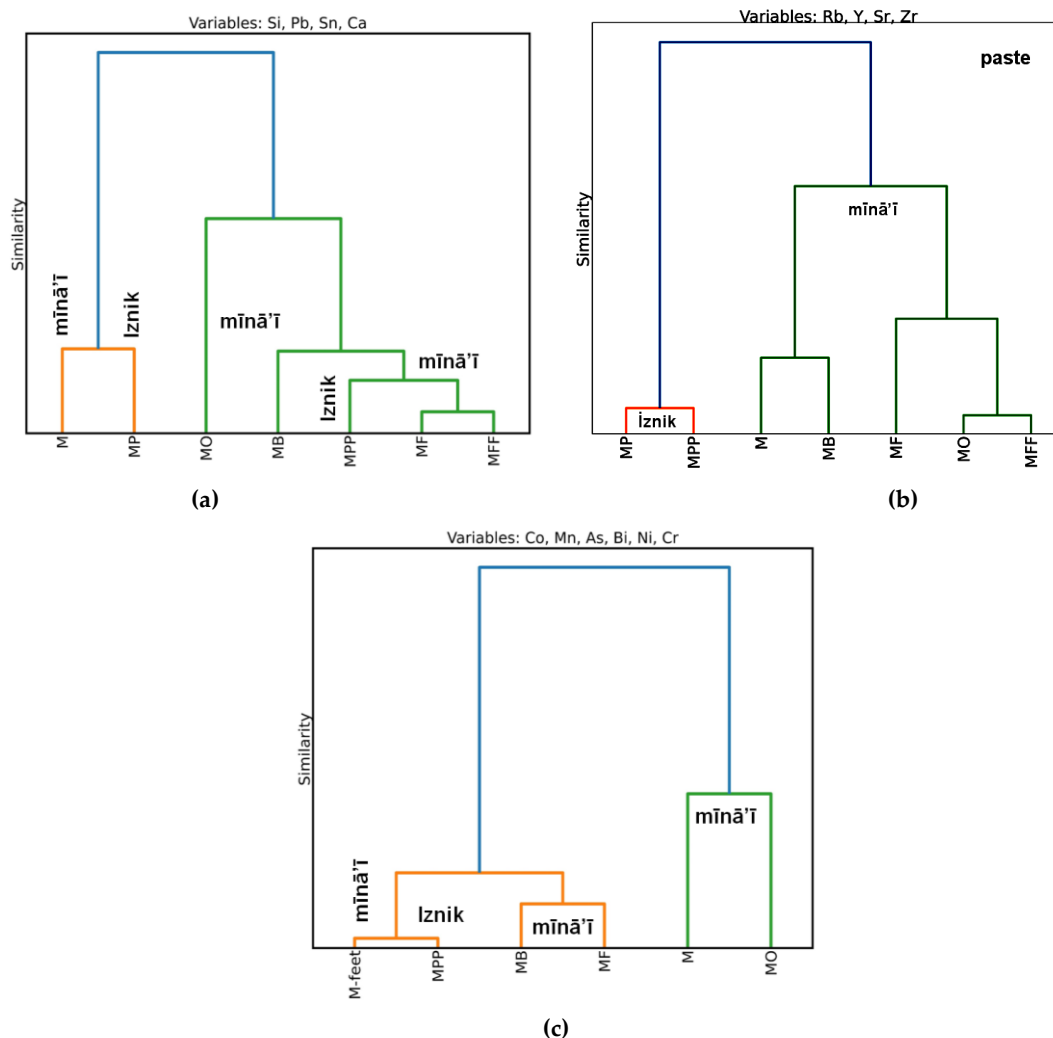


Figure 12. Hierarchical clustering classification of mīnā'ī and Īznik artifacts based on (a) major element content (Si, Pb, Sn, Ca) in the paste, (b) Rb, Y, Sr, and Zr impurities in the paste, and (c) elements associated with cobalt (Co, Mn, As, Bi, Ni, Cr) in the blue decoration.

463
464
465
466

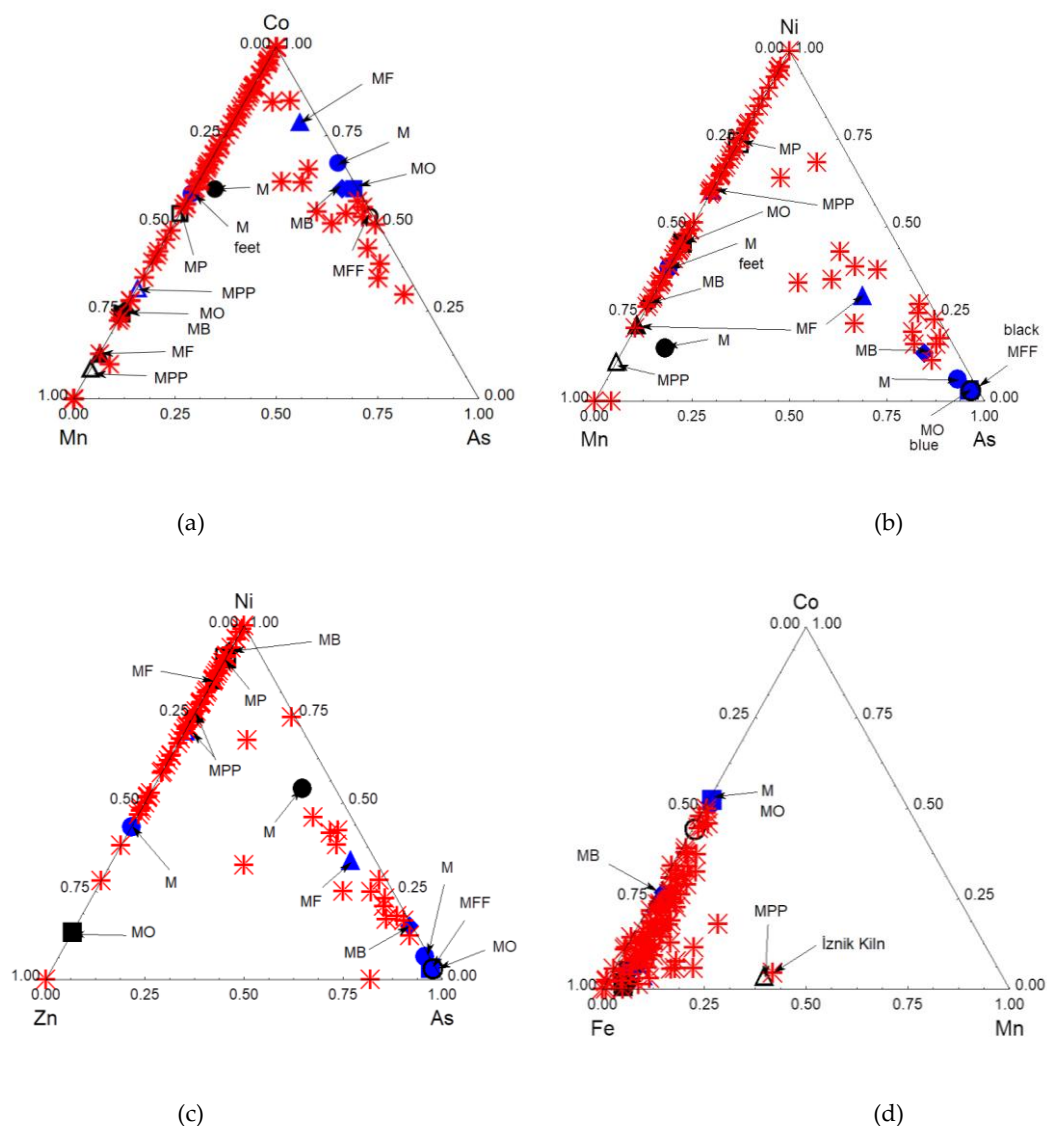


Figure 13. Comparison of the relative content of elements associated with cobalt in the blue glaze of mīnā'ī shards and Edirne and İznik tiles (red stars). A minor subgroup of İznik tiles, excavated from the İznik Tile Kilns site, clusters near the Co-As vertex, while other shards from the İznik Kilns and Edirne tiles [35,7167,7268,7369], sourced from various mosques, are positioned near the Co-Mn vertex.

5. Conclusions

Tin and lead were unexpectedly identified in the glassy phase (frit) cementing the mīnā'ī stone-paste body using pXRF. This finding was further confirmed by SEM-EDS analysis. Three distinct compositions of mīnā'ī paste were observed: (first M, and then MF, MFF, and MB on one hand, and MO on the other. Each composition exhibited different impurities, suggesting two separate sites or periods of production for the studied samples.

The ability of pXRF to efficiently distinguish between different types of mīnā'ī paste compositions (and their associated impurities) holds great promise for the non-invasive identification of objects originating from various production locations, workshops, cities, or eras. By analyzing both the major or minor elements in the pastes (Si, Pb, Sn, Ca) and the associated impurities (Rb, Y, Sr, Zr), Ward's hierarchical classification was able to

[effectively identify distinct groups.](#) A relationship was observed with later İznik fritware bodies, [although the classification remains inconclusive.](#)

Regarding the [blue-colored decoration which is characteristic of Islamic productions,](#) classification using the pXRF signal of cobalt and associated elements [\(Mn, As, Bi, Ni, Cr\) differentiates also very well](#) the M and MO mīnā'ī shards from the others. This finding emphasizes the importance of conducting [a series](#) of pXRF measurements on a much larger sample corpus. [Different types of black pigments were identified, including chromite, spinel, and cobalt-containing phases.](#)

Raman analyses using a blue laser indicate [for the first time](#) the presence of boron in blue-painted enamel, originating from the [specific composition](#) of Kashan cobalt ores. ~~Different types of black pigments were identified, including chromite, spinel, and cobalt.~~

The thinness of the painted enamel decoration makes Raman microspectroscopy-capable of analyzing very small volumes—one of the most effective techniques for characterizing the technical features of the decoration. [Variations in the polymerization index and the wavenumber of the center of gravity of the SiO₄ stretching mode indicate that painted enamels of different colors have distinct compositions, with varying PbO and B₂O₃ content. These differences require different firing temperatures and, consequently, multiple firing cycles. This complex firing chaîne opératoire is undoubtedly at the origin of the exceptional novelty of the enameled decoration found in mīnā'ī ware.](#)

[This innovative technology was later adopted by İznik potters two centuries after its initial development. However, the precise relationship between Seljuk and Ottoman potters remains an open question.](#)

Supplementary Materials: The following supporting information can be downloaded at: www.mdpi.com/xxx/s1, Table S1: pXRF data.

Author Contributions: Conceptualization, P.C.; methodology, P.C., A.-T.N. and G.S.F.; validation, P.C., and G.S.F.; investigation, P.C., X.G. and A.-T.N.; resources, X.X.; data curation, P.C., A.-T.N., X.G. and G.S.F.; writing—original draft preparation, P.C., and G.S.F.; writing—review and editing, P.C., X.G. and G.S.F.; visualization, P.C., and G.S.F.; s. All authors have read and agreed to the published version of the manuscript.

Funding: This research received no external funding.

Institutional Review Board Statement: Not applicable.

Informed Consent Statement: Not applicable.

Data Availability Statement: All data included in paper and Supplementary Information.

Acknowledgments: Mrs L. Soustiel is kindly acknowledged for the loan of shards from her collection.

Conflicts of Interest: The authors declare no conflicts of interest.

Appendix A

Table A1a. Local compositions (at %) measured by SEM-EDS for different spots on the body fracture with 400x magnification (~300x250 μm² area).

Shard	O	Si	Al	Mg	Na	K	Ca	P	S	Cl	Pb	Sn	Pb/Sn	Fe	Ti	Co	Cr
MPP1	66.3	19.29	2.85	0.31	5.48	0.52	0.29	0.43	0.4	0.56	3.22	0.31	10.4	0.02	-	-	-
MPP2+	73.75	9.26	4.38	0.62	2.42	0.36	1.22	4.26	0.98	0.52	2.13	0.04	53.2	0.03	0.03	-	-
MPP3	61.52	31.98	1.65	0.24	2.38	0.49	0.77	0.43	0.17		0.23	-	-	0.15	-	-	-
MP1 ^a	55.77	37.8	1.21	0.38	1.49	0.41	0.99	0.4	0.18	0.4	0.23	-	-	0.55	0.05	-	0.15
MP2	57.64	35.77	1.21	0.31	1.42	0.35	1.26	0.72	0.19	0.31	0.54	0.05	10.8	0.21	0.03	-	-
MO1 ^b	60.41	25.04	3.49	1.33	4.16	1.03	0.9	0.17	0.13	0.25	1.85	0.38	4.86	0.53	0.01	0.19	0.13
MO2	67.87	20.57	4.6	1.04	3.33	0.54	0.35	0.10	0.12	0.15	1.15	0.13	8.84	0.02	0.02	-	-
MFF1	55.82	25.58	3.61	1.68	6.04	1.11	1.30	0.15	0.18	0.52	2.6	1.23	2.1	0.15	0.02	-	-
MFF2	57.66	28.09	5.69	0.81	4.35	0.95	1.18	0.15	0.14	0.10	-	-	-	0.58	0.22	-	0.08

MFF3 ^c	57.69	27.06	5.54	1.24	3.12	1.26	0.86	0.14	0.15	0.28	1.89	0.39	4.85	0.23	0.03	0.14	-
MF1	63.68	25.52	4.34	0.55	3.74	0.95	0.41	0.14	0.08	0.16	-	-	-	0.21	0.23	-	-
MF2	67.56	18.37	3.61	0.64	2.81	1.16	1.32	0.65	0.23	0.26	1.17	1.89	0.61	0.29	0.04	-	-

+ magnification: 2000x; ^a: close to the black glaze; ^b close to the blue glaze; ^c close to the blue glaze.

Table A1b. Local compositions (at %) measured by SEM-EDS at different spots on the MPP shard decoration.

Shard	Color	O	Si	Al	Mg	Na	K	Ca	P	S	Cl	Pb	Sn	Pb/Sn	Fe	Ti	Cu	Co
MPP	Blue1 ^a	68.93	17.38	3.44	0.4	4.86	0.36	0.37	0.69	0.41	0.47	2.37	0.29	8.17	0.04	0.01	0.01	-
	Blue2 ^b	72.04	13.59	7.27	0.59	3.66	0.18	0.06	0.18	0.30	0.31	1.5	0.2	7.5	0.02	-	0.02	-
	Blue3 ^b	69.99	12.99	9.86	0.75	3.64	0.33	0.14	0.25	0.33	0.35	1.34	0.14	9.57	0.01	-	0.06	-
	Black1 ^a	70.75	14.27	5.84	0.38	2.1	0.41	1.03	2.41	0.69	0.46	1.41	0.08	17.62	0.07	0.04	0.02	0.03
	Black2 ^b	71.03	15.35	7.72	0.58	2.91	0.51	0.28	0.45	0.62	0.22	0.23	0.02	11.5	0.04	0.01	0.02	-

a: magnification 150x; b: magnification 400x;

References

- Crowe, Y. Change in style of Persian ceramics in the last part of 7/13th c. *Rivista degli studi orientali* **1985**, *59*(1/4), 47-55.
- Soustiel, J. La Céramique Islamique—Le Guide du Connaisseur; Office du Livre; Editions Vilo: Fribourg, Switzerland, 1985.
- Soustiel, J.; Porter, Y. Tombeaux de Paradis: Le Shâh-e Zende de Samarcande et la Céramique Architecturale d'Asie Centrale; Editions d'Art Monelle Hayot: Saint-Rémy-en-l'Eau, France, 2003.
- Watson, O. Ceramics From Islamic Lands-The Al-Sabah Collections, Thames & Hudson: London, UK, 2004, p.363.
- Mason, R.; Tite, M.; Paynter, S.; Salter, C. Advances in Polychrome Ceramics in Islamic World of the 12th Century AD. *Archaeometry* **2001**, *43*(2), 191-209.
- Mason, R. Shine Like the Sun; Lustre Painted and Associated Pottery from the Medieval Middle East, Mazda Publishers: Costa Mesa, CA, USA, 2004, p.131.
- McClary, R.P. A New Approach to Minā'ī Wares: Chronology and Decoration. *Persica* **2017**, 1-20. https://eprints.whit-rose.ac.uk/141057/1/McClary_Mina_i_Persica_2016.pdf
- François, V. Les Seldjoukides, médiateurs des importations de céramiques perses à Byzance, Byzance et l'Asie: 7e Symposium Byzantinon, Dec. 1997, *Byzantinische Forschungen: Inter. Zeitsc. Byzantinistik*, **1999**, *25*, 101-109.
- Lane, A. Early Islamic Pottery: Mesopotamia, Egypt and Persia, Faber and Faber: London, UK, 1947.
- Wen, R.; Pollard, A. The pigments applied to Islamic Minā'ī Wares and the correlation with Chinese Blue-and-White porcelain. *Archaeometry* **2015**, *58*(1), 1-16. <https://doi.org/10.1111/arc.12143>
- Sheikh, S.Z. Chinese Influence in Persian Manuscript Illustrations. *Int. J. of Multidisciplinary and Current research* **2017**, *5*.
- Loukonine, V.; Ivanov, A. *Persian Miniatures 120 illustrations*. Parkstone International: New York, 2023.
- Porter, Y. *Painters, Paintings and Books: An Essay on Indo-Persian Technical Literature, 12-19th Centuries*. Routledge: London, 2020.
- Allan, J. Abū'l Qāsim's Treatise on Ceramics. *Iran*, **1973**, *11*, 111-120.
- Holakoei, P. A Mediaeval Persian Treatise on Coloured and Enamelled Glass: Bayan Al-Sana'at. *Iran* **2016**, *54*, 95-106.
- Nikbakht, T.; Montazerzohouri, M. Characterization of historical minā'ī and colorful luster glaze ceramics, using ionoluminescence technique. *J. Luminescence* **2021**, *231*, 117769. <https://doi.org/10.1016/j.jlumin.2020.117769>
- Colomban, P.; Simsek Franci, G. Timurid, Ottoman, Safavid and Qajar Ceramics: Raman and Composition Classification of the Different Types of Glaze and Pigments. *Minerals* **2023**, *13*, 977. <https://doi.org/10.3390/min13070977>
- Holakoei, P.; de Lapérouse, J.-F.; Carò, F.; Röhrs, S.; Franke, U.; Müller-Wiener, M.; Reiche, I. Non-invasive scientific studies on the provenance and technology of early Islamic ceramics from Afrasiyab and Nishapur." *J. Archaeol. Sci.: Rep.* **2019**, *24*, 759-772. <https://doi.org/10.1016/j.jasrep.2019.02.029>
- Valiulina, S. Iranian Glazed Ceramics of the 12th—Beginning of the 13th Centuries in the Volga Bulgaria. *Heritage* **2021**, *4*, 3712–3730. https://www.academia.edu/download/90581878/heritage_04_00204.pdf
- Matin, M. Tin-based opacifiers in archaeological glass and ceramic glazes: a review and new perspectives." *Archaeol. & Anthropol. Sci.* **2019**, *11*, 1155-1167. <https://doi.org/10.1007/s12520-018-0735-2>
- Yazdani, M. The identification of black painted colorant in mina'i ceramic based on structural investigation and ancient treatise. *J. Color Sci. & Technol.* **2020**, *14*(3), 223-235.
- Soustiel, L. *L'Orient des Collectionneurs. Florilège d'Orient 4*, Laure Soustiel – Arts de l'Islam et de l'Inde: Aix-en-Provence, 2022.
- Baer, E. Metalwork in Medieval Islamic Art, State University of New York Press: Albany, USA, 1983.
- Irmawati J.M. Bird Symbolism in Persian Mysticism Poetry. *Inter. Rev. Humanities Stud.* **2019**, *4*(2), 695-716.
- Available on-line <https://sayisalkitap.qulto.eu/#/record/9789756959329> (accessed 7th December 2024).
- Denny, W.B. *İznik La Céramique Turque et l'Art Ottoman*; Citadelles and Mazenod: Paris, France, 2004.
- Dastjerdi, M.B. The Phoenix Motif during the Decline of the Sassanid Empire (600-700AD). Master's thesis, University of Malaya, Malaysia, 2017.

28. Barsam, M., Salehi Kakhki, A. and Saeedi Anaraki, F. Comparative analysis of form and composition, Minai wares motifs of the Jame' a mosque of Isfahan with two pictures of Varqa and Gulshah. *pazhoheshha-ye Bastan shenasi Iran*, **2023**, 12(35), 273-303. 570
29. Rohani, N. Strange Animals and Creatures in Islamic Miniatures: Focusing on Miniatures of the Conference of the Birds. *J. History Cult. & Art Res.* **2017**, 6(4), 112-126. <https://core.ac.uk/download/pdf/207885750.pdf> 572
30. Burlot, J.; Gallet, X.; Simsek Franci, G.; Bellot-Gurlet, L.; Colomban, P. Non-Invasive On-site pXRF Analysis of Coloring Agents, Marks and Glazes: Variability and Representativity of Measurements on Qing porcelain. *Colorants* **2023**, 2, 42–57. 574
<https://doi.org/10.3390/colorants2010004>. 576
31. Colomban, P.; Franci, G.S.; Gallet, X. Non-Invasive Mobile Raman and pXRF Analysis of Armorial Porcelain with the Coat of Arms of Louis XV and others Enamelled in Canton: Analytical Criteria for Authentication. *Heritage* **2024**, 7, 4881–4913. 577
<https://doi.org/10.3390/heritage7090231>. 578
32. Available online: <https://xrfcheck.bruker.com/InfoDepth> (accessed on 9 July 2024). 580
33. Colomban, P.; Simsek Franci, G.; Gironde, M.; d'Abriègeon, P.; Schumacher, A.-C. pXRF Data Evaluation Methodology for On-Site Analysis of Precious Artifacts: Cobalt Used in the Blue Decoration of Qing Dynasty Overglazed Porcelain Enamelled at Customs District (Guangzhou), Jingdezhen and Zaobanchu (Beijing) Workshops. *Heritage* **2022**, 5, 1752–1778. 581
<https://doi.org/10.3390/heritage5030091>. 582
34. Colomban, P.; Calligaro T.; Vibert-Guigue C.; Liem N.Q.; Edwards, H.G. Accrochage des dorures sur les céramiques et tesselles anciennes. *Revue d'Archéométrie-Archeosciences* **2006**, 29, 7-20. <https://doi.org/10.4000/archeosciences.424> 585
35. Arli, B.D.; Colomban, P.; Kaya, S.; Simsek, G., On-site pXRF analysis of body, glaze and colouring agents of the tiles at the excavation site of İznik kilns. *J. Eur. Cer. Soc.* **2019**, 39(6), 2199-2209. <https://doi.org/10.1016/j.jeurceramsoc.2019.01.050> 587
36. Oudbashi, O.; Emami, S.M.; Davami, P. Bronze in archaeology: a review of the archaeometallurgy of bronze in ancient Iran. Copper alloys-early applications and current performance-enhancing processes, in *Copper Alloys: Early Applications and Current Performance - Enhancing Processes*, Collini L. Ed, ch. 7, Interopen-Intech: Rijeka, Croatia **2012**, pp.161-186. 589
37. Khalil, W. and Kravchenko, S., "Minai" ceramics from Azak. *Egyptian Journal of Archaeological and Restoration Studies* **2016**, 6(2), 151-171. 592
38. Koleini, K.; Colomban, P.; Doosti, N.; Niakan, L. Glass finds from the elite house of Roue, a Sasanian city building in western Iran: Composition and classification using XRF and Raman spectroscopy, *Heritage*, **2024**, 7, 6137–6150. <https://doi.org/10.3390/heritage7110288>. 594
39. Kissin, S.A. Five element (Ni-Co-As-Ag-Bi) veins. *Geosci. Can.* **1992**, 19, 113–124. Available online: <https://journals.lib.unb.ca/index.php/gc/article/view/3768/4282/> (accessed on 15 December 2019). 595
40. Colomban, P.; Kirmızı, B.; Simsek Franci, G. Cobalt and Associated Impurities in Blue (and Green) Glass, Glaze and Enamel: Relationships between Raw Materials, Processing, Composition, Phases and International Trade. *Minerals* **2021**, 11, 633. 597
<https://doi.org/10.3390/min11060633>. 599
41. Ladame, G. Les ressources métallifères de l'Iran. *Schweiz. Mineral. Petrogr. Mitt.* **1945**, 25, 165–298. 602
42. Matin, M.; Pollard, A.M. From ore to pigment: A description of the minerals and experimental study of cobalt ore processing from the Kāshān mine, Iran. *Archaeometry* **2017**, 59, 731–746, doi:10.1111/arc.12272. 603
43. Matin, M.; Pollard, A.M. Historical accounts of cobalt ore processing from the Kāshān mine, Iran. *Iran* **2015**, 53, 171–183. 604
44. Colomban, P.; Truong, C. Non-destructive Raman study of the glazing technique in lustre potteries and faience (9–14th centuries): silver ions, nanoclusters, microstructure and processing. *J. Raman Spectrosc.* **2004**, 35(3), 195-207. 605
<https://doi.org/10.1002/jrs.1128> 606
45. Colomban, P. The use of metal nanoparticles to produce yellow, red and iridescent colour, from bronze age to present times in lustre pottery and glass: solid state chemistry, spectroscopy and nanostructure. *J. Nano Res.* **2009** 8, 109-132. 607
<https://www.scientific.net/JNanoR.8.109> 608
46. Colomban, P.; Milande, V.; Le Bihan, L. On-site Raman analysis of İznik pottery glazes and pigments. *J. Raman Spectrosc.* **2004**, 35, 527–535. <https://doi.org/10.1002/jrs.1163S>. 609
47. Bersani, D., and Lottici, P. P. (2016) Raman spectroscopy of minerals and mineral pigments in archaeometry. *J. Raman Spectrosc.*, 47: 499–530. doi: [10.1002/jrs.4914](https://doi.org/10.1002/jrs.4914). 610
48. Middleton, A.P.; Edwards, H.G.M.; Middleton, P.S.; Ambers, J. Identification of anatase in archaeological materials by Raman spectroscopy: implications and interpretation. *J. Raman Spectrosc.* **2005**, 36(10), 984-987. <https://doi.org/10.1002/jrs.1394> 611
49. Sun, J.; Wu, Z.; Cheng, H.; Zhang, Z.; Frost, R.L. A Raman spectroscopic comparison of calcite and dolomite. *Spectrochimica Acta Part A: Mol. Biomol. Spectrosc.* **2014**, 117, 158-162. <https://doi.org/10.1016/j.saa.2013.08.014> 612
50. Berenblut, B.J.; Dawson, P.; Wilkinson, G.R. The Raman spectrum of gypsum. *Spectrochimica Acta Part A: Mol. Spectrosc.* **1971** 27(9), 1849-1863. [https://doi.org/10.1016/0584-8539\(71\)80238-6](https://doi.org/10.1016/0584-8539(71)80238-6) 613

51. Colombari, P.; Kirmizi, B. Non-invasive on-site Raman study of polychrome and white enamelled glass artefacts in imitation of porcelain assigned to Bernard Perrot and his followers. *J. Raman Spectrosc.* **2020**, *51*(1), 133-146. <https://doi.org/10.1002/jrs.5745>
52. Frost, R.L. An infrared and Raman spectroscopic study of natural zinc phosphates. *Spectrochimica Acta Part A: Mol. Biomol. Spectrosc.* **2004**, *60*(7), 1439-1445. <https://doi.org/10.1016/j.saa.2003.08.009>
53. Colombari, P. Polymerization degree and Raman identification of ancient glasses used for jewellery, ceramics enamels and mosaics. *J. Non-Crystalline Solids*, **2003**, *323*(1-3), 180-187. [https://doi.org/10.1016/S0022-3093\(03\)00303-X](https://doi.org/10.1016/S0022-3093(03)00303-X)
54. Colombari, P.; Tournié, A.; Bellot-Gurlet, L. Raman Identification of glassy silicates used in ceramic, glass and jewellery: a tentative differentiation guide. *J. Raman Spectrosc.* **2006**, *37*(8), 841-852. <https://doi.org/10.1002/jrs.1515>
55. Zhao, Y.; Chen, S.; Huang, Y.; Zhao, J.; Tong, X.; Chen, X. U-Pb ages, O isotope compositions, Raman spectrum, and geochemistry of cassiterites from the Xi'ao copper-tin polymetallic deposit in Gejiu District, Yunnan Province. *Minerals*, **2019**, *9*(4), 212. <https://doi.org/10.3390/min9040212>
56. Colombari, P. Raman Spectrometry, A unique tool for on-site analysis and identification of ancient ceramics and glasses. *Mater. Res. Soc. Symp. Proc.* **2005**, *852*, OO8.3.1. <https://doi.org/10.1557/PROC-852-OO8.3>
57. Kamura, S.; Tani, T.; Matsuo, H.; Onaka, Y.; Fujisawa, T.; Unno, M. New probe for porcelain glazes y luminescence at Near-Infrared excitation. *ACS Omega* **2021**, *6*, 7829-7833. DOI: 10.1021/acsomega.1c00322
58. Tite, M.; Pradell, T.; Shortland, A. Discovery, production and use of tin-based opacifiers in glasses, enamels and glazes from the late iron age onwards: A reassessment. *Archaeometry* **2008**, *50*(1), 67-84. <https://doi.org/10.1111/j.1475-4754.2007.00339.x>
59. Burlot, J.; Vangu, D.; Bellot-Gurlet, L.; Colombari, P. [Raman Identification of pigments and opacifiers: Interest and limitation of multivariate analysis by comparison with solid state spectroscopical approach II. Arsenic-based opacifiers and relation with cobalt ores](https://doi.org/10.1002/jrs.6612), *J Raman Spectrosc* **2024**, *55*(2), 184-199. <https://doi.org/10.1002/jrs.6612>
60. Colombari, P.; Ngo, A.-T.; Fournerie, N. Non-Invasive Raman Analysis of 18th Century Chinese Export/Armorial Overglazed Porcelain: Identification of the Different Enameling Techniques. *Heritage* **2022**, *5*, 233-259. <https://doi.org/10.3390/heritage5010013>
61. Hassan, H.K.; Torell, L.M.; Börjesson, L.; Doweidar, H. Structural changes of B₂O₃ through the liquid-glass transition range: A Raman-scattering study. *Phys. Rev. B* **1992**, *45*, 12797. <https://doi.org/10.1103/PhysRevB.45.12797>.
62. Ciceo-Lucatel, R.; Ardelean, R. FT-IR and Raman study of silver lead borate-based glasses. *J. Non-Crystall. Solids* **2007**, *353*, 2020-2024. <https://doi.org/10.1016/j.jnoncrysol.2007.01.066>
63. Satyanarayana, T.; Kityk, I.V.; Piasecki, M.; Bragiel, P.; Brik, M.G.; Gandhi, Y.; Veeraiah, N. Structural investigations on PbO-Sb₂O₃-B₂O₃:CoO glass ceramics by means of spectroscopic and dielectric studies. *J. Phys. Condens. Matter* **2009**, *21*, 245104. DOI 10.1088/0953-8984/21/24/245104
64. Moshkina, E.; Gudim, I.; Temerov, V.; Krylov. Temperature-dependent absorption lines observation in Raman spectra of SmFe₃(BO₃)₄ ferroborate. *J. Raman Spectrosc.* **2018**, *49*, 1732-1735. DOI: 10.1002/jrs.5430
65. Maggetti, M.; D'Albis, A. Phase and compositional analysis of a Sèvres soft paste porcelain plate from 1781, with a review of early porcelain techniques. *Eur. J. Mineral.* **2017**, *29*, 347-367. <https://doi.org/10.1127/ejm/2017/0029-2627>
66. Burlot, J.; Colombari, P.; Bellot-Gurlet, L.; Lemasson, Q.; Pichon, L. Non-invasive analyze of boron and lithium in 18th century Chinese porcelain enamel and glaze: A PIXE/PIGE study. *J. Eur. Ceram. Soc.* **2024**, *44*, 116746.
67. Tite, Michael S.; Shortland, A. J.; Schibille, N.; Degryse, P. New Data on the Soda Flux Used in the Production of I znik Glazes and Byzantine Glasses. *Archaeometry* **2016**, *58*(1), 57-67. <https://doi.org/10.1111/arcm.12156>
68. Ma, H.; Henderson, J.; Cui, J.; Chen, K. Glassmaking of the Qing Dynasty: a review, new data, and new insights. *Adv. Archaeo-materials* **2020**, *1*(1), 27-35. <https://doi.org/10.1016/j.aia.2020.11.001>
- 65-69. Pinto, A.; Sciau, P.; Zhu, T.Q.; Zhao, B.; Groenen, E.S. Raman study of Ming porcelain dark spots: Probing Mn-rich spinels. *J. Raman Spectrosc.* **2019**, *50*, 711-719. DOI: 10.1002/jrs.5568
- 66-70. Froment, F.; Tournié, A.; Colombari, P. Raman identification of natural red to yellow pigments: Ochre and iron-containing ores. *J. Raman Spectrosc.* **2008**, *39*(5), 560-568. *J. Raman Spectrosc.* **2008**, *39*, 560-568.

- 67-71. Demirsar Arli, B.; Simsek Franci, G.; Kaya, S.; Arli, H.; Colombar, P. Portable X-ray Fluorescence (p-XRF) Uncertainty Estimation for Glazed Ceramic Analysis: Case of Iznik Tiles, *Heritage*, **2020**, *3*, 1302-1329; <https://doi.org/10.3390/heritage3040072>. 667
668
669
72. Simsek, G.; Unsalan, O.; Bayraktar, K.; Colombar, P. On-site pXRF analysis of glaze composition and colouring agents of “Iznik” tiles at Edirne mosques (15th and 16th-centuries), *Ceramics International*, 2019, *45*(1), 595-605. 670
<https://doi.org/10.1016/j.ceramint.2018.09.213>. 671
672
- 68-73. 673
674
675

Disclaimer/Publisher’s Note: The statements, opinions and data contained in all publications are solely those of the individual author(s) and contributor(s) and not of MDPI and/or the editor(s). MDPI and/or the editor(s) disclaim responsibility for any injury to people or property resulting from any ideas, methods, instructions or products referred to in the content. 676
677
678